Multiple polaron quasiparticles with dipolar fermions in a bilayer geometry

Antonio Tiene [1], Andrés Tamargo Bracho,[1] Meera M. Parish [2,3] Jesper Levinsen [2,3] and Francesca Maria Marchetti [1]

[1]*Departamento de Física Teórica de la Materia Condensada & Condensed Matter Physics Center (IFIMAC),*
Universidad Autónoma de Madrid, Madrid 28049, Spain
[2]*School of Physics and Astronomy, Monash University, Victoria 3800, Australia*
[3]*ARC Centre of Excellence in Future Low-Energy Electronics Technologies, Monash University, Victoria 3800, Australia*

We study the Fermi polaron problem with dipolar fermions in a bilayer geometry, where a single dipolar particle in one layer interacts with a Fermi sea of dipolar fermions in the other layer. By evaluating the polaron spectrum, we obtain the appearance of a series of attractive branches when the distance between the layers diminishes. We relate these to the appearance of a series of bound two-dipole states when the interlayer dipolar interaction strength increases. By inspecting the orbital angular-momentum component of the polaron branches, we observe an interchange of orbital character when system parameters such as the gas density or the interlayer distance are varied. Furthermore, we study the possibility that the lowest energy two-body bound state spontaneously acquires a finite center-of-mass momentum when the density of fermions exceeds a critical value, and we determine the dominating orbital angular momenta that characterize the pairing. Finally, we propose to use the tunneling rate from and into an auxiliary layer as an experimental probe of the impurity spectral function.

I. INTRODUCTION

Over the last two decades, significant progress has been made in manipulating ultracold gases of dipolar atoms and molecules. The surge in experimental activity in this field is motivated by the expectation that the anisotropic and long-range nature of dipole-dipole interactions can lead to exotic states of matter [1–3]. Significant progress has already been made with dipolar gases of highly magnetic atoms such as Cr [4,5], Dy [6,7], and Er [8,9], where the achievement of quantum degeneracy has allowed the investigation of droplets, supersolids and other quantum phenomena [10]. However, in order to access the regime of strong dipole-dipole interactions, one requires other cold-atom platforms such as Rydberg atoms [11] or heteronuclear molecules [12,13].

Fermionic polar molecules in layered geometries are particularly promising for realizing quantum phases with strong and tunable dipolar interactions. By confining dipolar molecules to two-dimensional (2D) layers, inelastic losses are suppressed, while the sign and strength of the dipolar interactions can be precisely controlled [14]. Degenerate 2D Fermi gases have already been achieved with KRb [15,16] and NaK [17,18], while other molecules, including LiCs [19,20] and NaLi [21], are also being explored. Moreover, recent experiments with ultracold KRb molecules have demonstrated the possibility to image and control multiple layers individually [22], thus expanding the range of scenarios that can be explored with 2D dipolar gases.

From a theoretical standpoint, dipole-dipole interactions are expected to generate ordered phases of fermions in layered geometries. Of particular interest is the configuration where all dipole moments are aligned perpendicularly to the confining planes, such that the system has rotational symmetry. In the case of a single layer, intralayer superfluid *p*-wave

pairing can be driven by dressing polar molecules with a microwave field [23,24]. Furthermore, density-wave instabilities with dipolar fermions have been proposed [25–27], including the spontaneous appearance of a stripe phase [28] and Wigner crystallization [29] at sufficiently high densities or strong interactions. In the case of bilayers, in addition to density-wave instabilities [30], new interlayer bound pairs can arise due to the attractive part of the dipolar interaction [31–34]. Such pairing and associated interlayer superfluidity has been studied in the case of both balanced [25,33,35] and imbalanced populations [36]. The latter includes the possibility of realizing a Fulde-Ferrell-Larkin-Ovchinnikov (FFLO) modulated pairing phase [37]. Most notably, the stability of the FFLO state can be enhanced by the long-range character of the interlayer dipolar interaction, where different partial waves contribute to the pairing order parameter.

In this work, we consider the limit of extreme population imbalance for dipolar fermions in a bilayer, as illustrated in Fig. 1. Specifically, we have an impurity problem, where a single dipolar particle in one layer interacts with a Fermi sea of identical dipolar fermions in a different layer. This so-called "Fermi-polaron" problem has previously been considered in Refs. [38,39] for the case of dipoles in a bilayer geometry,[1] and the general problem of an impurity in a 2D Fermi gas has been extensively studied in other 2D platforms such as ultracold atoms [41–46] and doped semiconductors [47–50]. Our scenario can be readily realized with polar molecules; however, note that our setup is quite general and could in principle apply to other dipoles such as Rydberg atoms. We consider two possible solutions of this problem. In the first,

―――――

[1]The "repulsive Fermi polaron" problem with dipolar fermions in a single layer geometry has been considered in Ref. [40].
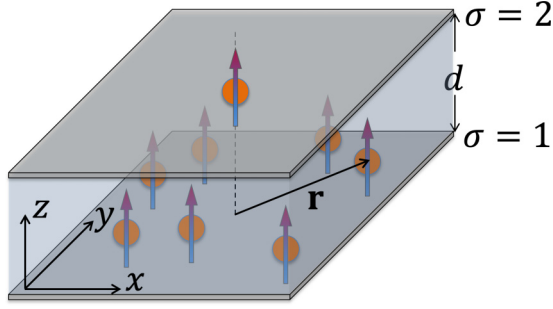
FIG. 1. Schematic representation of the bilayer geometry considered: a Fermi gas of dipoles (such as polar molecules) is confined in the bottom layer $\sigma = 1$, while a single dipole with the same perpendicular alignment is confined in the layer $\sigma = 2$, generating an impurity problem where two interlayer dipoles attract each other at short distances $r \lesssim d$ and repel each other at large distances $r \gtrsim d$ (see Fig. 2). Tunneling between the two layers is prevented by a barrier (blue filled region between the two layers).

we generalize the interlayer bound state between two dipoles to include the effects of an inert Fermi sea and how it blocks the occupation below the Fermi momentum. In the second, we consider the possibility of "polaron" quasiparticles, where the impurity is dressed by particle-hole excitations of the Fermi sea. Throughout, we compare our results with those previously obtained within a T-matrix formalism which focused on the limit of weak dipolar interactions [38].

By employing a variational ansatz, we evaluate the polaron spectrum to reveal that it is characterized by a series of attractive polaron branches, where the number of branches increases when the distance between the two layers decreases or the dipole moment increases. We associate the appearance of these polaron branches to the series of two-body bound states that, similarly to the 2D hydrogen atom [51], is characterized by a specific orbital angular-momentum component and a principal quantum number. In the limit of vanishingly small density of fermions, the attractive polaron energies recover those of the dipole-dipole bound states. By evaluating the orbital angular-momentum component of each polaron branch, we observe that the partial-wave character of the branches evolve and interchange when we either increase the Fermi density or, at a fixed density, we increase the bilayer distance.

In contrast with the well-studied case of contact impurity-medium interactions [52,53], a distinctive feature of finite-range dipole-dipole interactions is that the energy of the lowest-energy polaron branch can either redshift, i.e., lower its energy, with increasing Fermi density, or blueshift. We find that this depends on the precise value of the dipolar strength, a quantity related to the specific value of the dipole moment and the layer separation. We explain this qualitative different behavior in terms of the contribution of hole scattering in the polaron formation, which we find is particularly important for the dipolar potential.

Furthermore, we consider the possibility that the lowest dipole-dipole bound state spontaneously acquires a finite center-of-mass momentum when the density of the Fermi sea increases. Because of the long-range nature of the dipole-dipole interaction, this finite-momentum bound state mixes

different orbital angular-momentum components. We show that, while for small densities, s-wave pairing dominates close to the transition, for larger densities, the bound state acquires p- and d-wave components. These results agree with those found at finite but large imbalance in Ref. [37].

The paper is organized as follows: In Sec. II we introduce the model of identical dipolar fermions in a bilayer geometry, and we discuss the relevant length and energy scales including their typical values in current experiments for either strongly magnetic atoms or heteronuclear molecules. Section III describes the properties of the two-body interlayer bound states, generalized to the case where a Fermi gas in one of the layers acts to block the occupation of states below the Fermi sea. In Sec. IV we describe the spectral properties of the Fermi polaron, while in Sec. V we show that the polaron spectral function can be probed analogously to radio-frequency spectroscopy by introducing an auxiliary layer to the system. Conclusions and perspectives are gathered in Sec. VI.

II. MODEL

We investigate the configuration schematically represented in Fig. 1. A Fermi sea of dipoles (e.g., polar molecules) is confined in one layer, with index $\sigma = 1$, where the dipole moments of the molecules are aligned perpendicularly to the plane by an external field. Additionally, a single dipolar molecule with the same perpendicular alignment occupies layer $\sigma = 2$. The Hamiltonian describing the systems is (we set $\hbar = 1$ and the system area $\mathcal{A} = 1$)

$$\hat{H} = \sum_{\mathbf{k},\sigma} \epsilon_{\mathbf{k}} \hat{c}^{\dagger}_{\mathbf{k},\sigma} \hat{c}_{\mathbf{k},\sigma} + \sum_{\mathbf{k}\mathbf{k}'\mathbf{q}} V_{\mathbf{q}} \hat{c}^{\dagger}_{\mathbf{k}-\mathbf{q},1} \hat{c}^{\dagger}_{\mathbf{k}'+\mathbf{q},2} \hat{c}_{\mathbf{k}',2} \hat{c}_{\mathbf{k},1}, \quad (1)$$

where $\hat{c}^{\dagger}_{\mathbf{k},\sigma}$ ($\hat{c}_{\mathbf{k},\sigma}$) is the creation (annihilation) operator of a fermionic dipole with momentum $\mathbf{k}$ in layer σ. Dipoles in different layers have the same mass m and their kinetic energy is $\epsilon_{\mathbf{k}} = k^2/2m$.

In writing Eq. (1) we have implicitly assumed that the intralayer correlations are weak, such that the gas in layer 1 is in a Fermi-liquid phase where it can be treated as approximately noninteracting. This neglects the possibility of density instabilities which can occur in a (perpendicularly aligned) 2D dipolar Fermi gas with large dipole moments or high densities [28].

On the other hand, the second term in the Hamiltonian (1) describes the dipolar interaction between a molecule in layer 1 and one in layer 2. The interlayer dipolar potentials in real and momentum space are, respectively, given by [33,34,54]

$$V(\mathbf{r}) = D^2 \frac{r^2 - 2d^2}{(r^2 + d^2)^{5/2}}, \quad (2a)$$

$$V_{\mathbf{q}} = -2\pi D^2 q e^{-qd}, \quad (2b)$$

where $\mathbf{r}$ is the planar separation. Here d is the layer separation and D^2 is the dipolar interaction strength. Out of these variables it is profitable to introduce a dimensionless dipolar strength

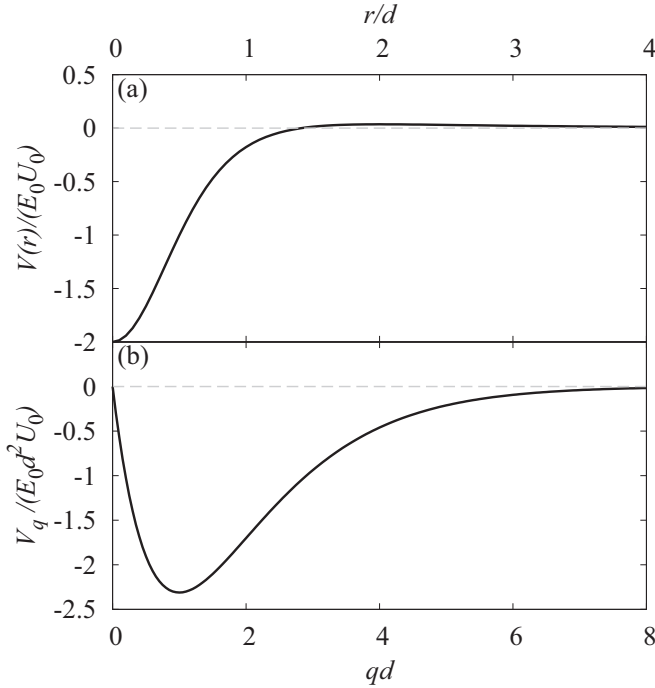$$U_0 = \frac{mD^2}{d} = \frac{D^2}{E_0 d^3}, \quad (3)$$

FIG. 2. Interlayer dipolar interaction potential, Eq. (2), in (a) real and (b) momentum space.

where $E_0 \equiv 1/md^2$ is the energy scale associated with the layer separation. We see that U_0 increases by either increasing the dipolar interaction strength or by moving the two layers closer to each other.

The interlayer dipolar potential is plotted in Fig. 2 in real and momentum space. As expected, in real space the potential is attractive at short distances $r \lesssim d$, where the dipoles are effectively arranged head-to-tail, while it is repulsive at large distances $r \gtrsim d$, where the dipoles are arranged side-by-side. Note that the interlayer potential has a vanishing zero-momentum contribution, i.e.,

$$V_{\mathbf{q}=0} = \int d\mathbf{r}\, V(\mathbf{r}) = 0.$$

This implies that the two-dipole bound state becomes very shallow when $U_0 \to 0$ [34], as discussed further in Sec. III.

The dipolar interaction strength D^2, which has the dimensions of energy times volume, is related to either the permanent magnetic dipole moment μ_m of a magnetic atom or to the dipole moment D_e of an atom or a molecule induced by an electric field [1]:

$$D^2 = \begin{cases} \frac{\mu_0}{4\pi}\mu_m^2 & \text{magnetic} \\ \frac{1}{4\pi\epsilon_0}D_e^2 & \text{electric}, \end{cases}$$

where μ_0 is the vacuum permeability and ϵ_0 the vacuum permittivity. Usually heteronuclear molecules with induced electric dipole moments display much stronger dipole-dipole interactions than atoms with a permanent magnetic moment. To quantify the dipolar interaction, it is convenient to

TABLE I. Typical values of the dipolar length a_{dd} in units of the Bohr radius $a_0 = 0.0529$ nm for the highly magnetic atom ^{164}Dy [3], and for the heteronuclear molecules KRb [1,14] and LiCs [56]. The corresponding value of the dimensionless dipolar interaction strength U_0 (3) is given in the second and third column for two different bilayer distances d. In the fourth column we have U_F (6) (which is independent of d) for a typical Fermi gas density $n \simeq 10^8$ cm^{-2}.

	$a_{dd}(a_0)$	$U_0(d=50\,\text{nm})$	$U_0(d=500\,\text{nm})$	U_F
^{164}Dy	130.7	0.4	0.04	0.07
KRb	2×10^3	6.3	0.6	1.1
LiCs	2×10^5	634.8	63.5	110

introduce the dipolar length a_{dd} [1,3]:[2]

$$D^2 = \frac{3a_{dd}}{m}. \tag{4}$$

For heteronuclear molecules, a_{dd} can be up to three orders of magnitude larger than for magnetic atoms. Typical values of a_{dd} for the highly magnetic atom ^{164}Dy and for the heteronuclear molecules KRb and LiCs are given in Table I. Furthermore, in current experiments, typically $d \simeq 500$ nm; however, very recently a new superresolution technique which localizes and arranges dipolar molecules on a sub-50 nm scale has been implemented [55]. The corresponding values of U_0 that can be achieved for both highly magnetic atoms and heteronuclear molecules are listed in Table I. Throughout this work we consider the dipoles to be structureless fermions such that we do not make a distinction between magnetic atoms or heteronuclear molecules.

The density n of dipoles in layer 1 is related to the Fermi momentum k_F by

$$k_F = \sqrt{4\pi n}. \tag{5}$$

From this, we can define a many-body dimensionless parameter U_F analogous to the dipolar strength U_0:

$$U_F = U_0 k_F d = U_0 \sqrt{\frac{2E_F}{E_0}} = mD^2 k_F. \tag{6}$$

This dimensionless interaction strength characterizes the extent of many-body correlations in the system. As discussed above, we neglect the intralayer interaction and assume an ideal Fermi gas in layer 1. Strictly speaking, this requires us to consider sufficiently small values of U_F such that there are no ordered phases. Specifically, in the case of perpendicular orientation of the dipole moments, it has been found that the translational symmetry is broken for $U_F \gtrsim 6$ towards the appearances of a stripe phase [28], while Wigner crystallization can occur for $U_F \gtrsim 25$ [29]. Nevertheless, to comprehensively characterize bound-state and polaron properties in the presence of a Fermi gas, we must extend our investigation to higher-density values. Therefore, to preserve the assumption of an ideal Fermi gas in layer 1, we implicitly assume that there is a small but finite temperature that induces the melting

---

[2]Note that Refs. [1,3] use a different definition of C_{dd} but the same definition of a_{dd}: $C_{dd}^{\text{Lehaye}} = 4\pi C_{dd}^{\text{Chomaz}} = 4\pi D^2 = 12\pi\frac{a_{dd}}{m}$.

TABLE II. Values of the dimensionless density parameters E_F/E_0 and $1/k_F d$ that can be accessed in experiments on dipolar Fermi gases with a bilayer distance d and a typical density of the Fermi gas $n \simeq 10^8$ cm^{-2}.

	$d = 50$ nm	$d = 500$ nm
E_F/E_0	0.015	1.6
$1/k_F d$	5.7	0.56

of the strongly correlated phases without strongly affecting the impurity physics.

Typically, the density of the 2D Fermi gas in experiments is $n \simeq 10^8$ cm^{-2}. This leads to values of U_F listed in the fourth column of Table I. We furthermore list typical values for the dimensionless parameters E_F/E_0 and $1/k_F d$ at different bilayer separation d in Table II.

III. DIMER STATES

Due to the attractive part of the dipolar interaction, two dipoles can form an interlayer bound state. In this section, we discuss the properties of this two-body bound (dimer) state, generalized to the case where the Fermi gas in layer 1 is inert and acts to block the occupation below the Fermi momentum k_F. We thus consider a general two-body state with a center-of-mass momentum $\mathbf{Q}$ described by

$$\big|M_2^{(\mathbf{Q})}\big\rangle = \sum_{\mathbf{k} > k_F} \eta_{\mathbf{k}}^{(\mathbf{Q})} \hat{c}_{\mathbf{Q}-\mathbf{k},2}^{\dagger} \hat{c}_{\mathbf{k},1}^{\dagger} |\text{FS}\rangle, \tag{7}$$

where the sum over the relative momenta $\mathbf{k}$ is restricted by Pauli blocking, $k > k_F$, while $|\text{FS}\rangle \equiv \prod_{\mathbf{q} < k_F} \hat{c}_{\mathbf{q},1}^{\dagger} |0\rangle$ describes the Fermi sea in layer 1, and $\eta_{\mathbf{k}}^{(\mathbf{Q})}$ is the two-body wave function. The energies E can then be found by solving the corresponding Schrödinger equation:

$$E\eta_{\mathbf{k}}^{(\mathbf{Q})} = (\epsilon_{\mathbf{k}} + \epsilon_{\mathbf{Q}-\mathbf{k}})\eta_{\mathbf{k}}^{(\mathbf{Q})} + \sum_{\mathbf{k}' > k_F} V_{|\mathbf{k}-\mathbf{k}'|}\eta_{\mathbf{k}'}^{(\mathbf{Q})}, \tag{8}$$

which can be readily solved by numerical diagonalization.

Before discussing the solution of Eq. (8), it is useful to classify the dimer states according to their orbital angular-momentum component. First, if the impurity momentum $Q = 0$, the system is rotationally symmetric, and angular momentum is a good quantum number. Furthermore, when $E_F = 0$, the center of mass and relative motion decouple, and therefore the energy at finite Q is simply related to the energy at $Q = 0$ via $E^{(Q)} = E^{(Q=0)} + Q^2/4m$, allowing us to take advantage of the rotational symmetry at $Q = 0$. The presence of the Fermi sea complicates matters because then the center-of-mass motion no longer decouples. Thus, for a dimer state where both $\mathbf{Q}$ and E_F are finite, the system is no longer rotationally invariant and orbital angular momentum is not conserved.

To proceed, we expand the dimer wave function as a Fourier series over the orbital angular-momentum basis $e^{i\ell\varphi}$:

$$\eta_{\mathbf{k}}^{(\mathbf{Q})} = \eta_{k\varphi}^{(Q)} = \sum_{\ell \in \mathbb{Z}} e^{i\ell\varphi} \tilde{\eta}_{k\ell}^{(Q)}, \tag{9}$$

where φ is the angle between $\mathbf{k}$ and $\mathbf{Q}$. The dimer Schrödinger equation (8) now reads

$$E\tilde{\eta}_{k\ell}^{(Q)} = (2\epsilon_{\mathbf{k}} + \epsilon_{\mathbf{Q}})\tilde{\eta}_{k\ell}^{(Q)} - \frac{kQ}{2m}\big(\tilde{\eta}_{k,\ell-1}^{(Q)} + \tilde{\eta}_{k,\ell+1}^{(Q)}\big)$$
$$+ \int_{k_F}^{\infty} \frac{dk'\,k'}{2\pi} \tilde{V}(k,k',\ell)\tilde{\eta}_{k'\ell}^{(Q)}. \tag{10}$$

Here, we have taken the continuum limit $\sum_{\mathbf{k}'} \to \int d\mathbf{k}'/(2\pi)^2$ and decomposed the interlayer potential in the orbital angular-momentum basis by using the fact that the potential is diagonal in angular momentum, i.e.,

$$\int_0^{2\pi} \frac{d\varphi}{2\pi} \frac{d\varphi'}{2\pi} e^{-i\ell\varphi} V_{|\mathbf{k}-\mathbf{k}'|} e^{i\ell'\varphi'} = \delta_{\ell\ell'}\tilde{V}(k,k',\ell), \tag{11}$$

where $\mathbf{k} = (k,\varphi)$ and $\mathbf{k}' = (k',\varphi')$. Note that the potential $\tilde{V}(k,k',\ell)$ is real.

As expected, Eq. (10) becomes diagonal in ℓ when $Q = 0$ since, in this limit, the orbital angular momentum is a good quantum number. Note also that, because the potential $\tilde{V}(k,k',\ell)$ is symmetric under the exchange $\ell \mapsto -\ell$, the eigenvectors for $\ell \neq 0$ can either be symmetric or antisymmetric solutions:

$$\tilde{\eta}_{k\ell}^{(\pm,Q)} = \frac{\tilde{\eta}_{k\ell}^{(Q)} \pm \tilde{\eta}_{k,-\ell}^{(Q)}}{2}, \tag{12}$$

where $\tilde{\eta}_{k0}^{(+,Q)} = \tilde{\eta}_{k0}^{(Q)}$, while $\tilde{\eta}_{k0}^{(-,Q)} = 0$. In terms of these, the Schrödinger equation reads ($\ell \geqslant 0$)

$$E\tilde{\eta}_{k\ell}^{(\pm,Q)} = (2\epsilon_{\mathbf{k}} + \epsilon_{\mathbf{Q}})\tilde{\eta}_{k\ell}^{(\pm,Q)} - \frac{kQ}{2m}\big(\tilde{\eta}_{k|\ell-1|}^{(\pm,Q)} + \tilde{\eta}_{k\ell+1}^{(\pm,Q)}\big)$$
$$+ \int_{k_F}^{\infty} \frac{dk'k'}{2\pi} \tilde{V}(k,k',\ell)\tilde{\eta}_{k'\ell}^{(\pm,Q)}. \tag{13}$$

One can see that the Schrödinger equation (10) now becomes block diagonal using the symmetric and antisymmetric dimer wave functions, i.e., the equations for $\tilde{\eta}_{k0}^{(Q)}$ and $\tilde{\eta}_{k\ell}^{(+,Q)}$ decouple from those for $\tilde{\eta}_{k\ell}^{(-,Q)}$, the former $l = 0$ states being in general the lowest-energy solutions.[3]

In the following two sections, we first analyze the two-body limit, i.e., the limit $E_F \to 0$ where there is a single particle in each of layers 1 and 2, and we study the appearance of additional bound dimer states when the interlayer dipolar strength U_0 increases. Then, in Sec. III B, we consider the effect of a finite density of fermions in layer 1 and how this can lead to the dimer spontaneously acquiring a finite center-of-mass momentum.

---

[3]Note that, as mentioned previously, the Schrödinger equation becomes diagonal in ℓ when either $Q = 0$ or $E_F = 0$, such that symmetric and antisymmetric solutions become degenerate.
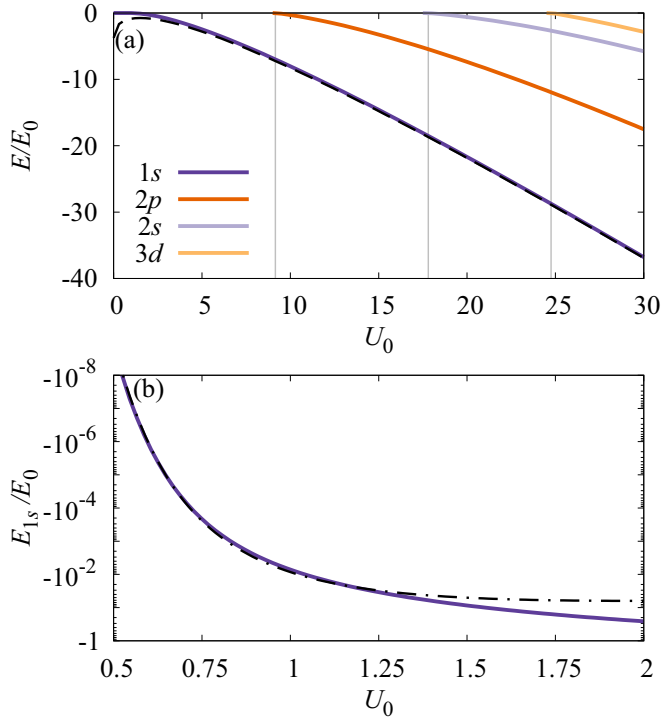
FIG. 3. Energies of the bound-state dimers at $E_F = 0$ and $Q = 0$ as a function of the dipolar interaction strength U_0. The energies are labeled with $n\ell$, where ℓ is the orbital angular momentum ($\ell = 0$ is s wave, $\ell = 1$ is p wave, and $\ell = 2$ is d wave) and n is the eigenvalue index, where $n \geqslant \ell + 1$. (a) Vertical (gray) lines are the binding thresholds for the $2p$, $2s$, and $3d$ states (see Table III). The black (dashed) line is the analytical expression (15) for E_{1s} valid for $U_0 \gg 1$. (b) U_0 dependence of E_{1s} for small values of U_0 and comparison with the analytical expression (14) valid for $U_0 \ll 1$ [black (dot-dashed)].

A. Vacuum dimer

As explained above, in the absence of a Fermi sea in layer 1, the center-of-mass motion and relative motion decouple. We therefore solve the two-body problem at $Q = 0$. The dimer states can be labeled by the orbital angular momentum ℓ and the eigenvalue index n (where increasing values of n indicate larger energies eigenstates), which we assume to be $n \geqslant \ell + 1$, in analogy with the 2D hydrogenic atom [51].

We plot in Fig. 3 the energies of the dimer states for increasing values of U_0, i.e., for either increasing values of the dipole moments D^2 or smaller bilayer distances d. As expected, the $1s$ state is always bound for $U_0 \neq 0$, even if it becomes very shallow when $U_0 \ll 1$, i.e., the binding energy goes exponentially to zero. This has been already analyzed by Ref. [34] and traced back to the fact that the interlayer dipolar potential has a vanishing zero-momentum contribution,

TABLE III. Threshold values of U_0 for the binding of excited dimer states.

	$2p$	$2s$	$3d$	$3p$	$4f$	$3s$	$4d$	...
U_0	9.2	17.8	24.7	35	48	52	59.5	...

in which case one cannot use Landau's formula for the energy of the bound state $E_{1s} \propto -\exp[4\pi / \int d\mathbf{r} \, V(r)]$. Instead, Ref. [34] found an approximation for the $1s$ energy when $U_0 \ll 1$ by employing the Jost function formalism, leading to

$$E_{1s} \underset{U_0 \to 0}{\simeq} -E_0 e^{-\frac{8}{U_0^2}\left[1 - U_0 + \frac{U_0^2}{4}\left(\frac{5}{2} + \gamma - \ln 2\right)\right]}, \quad (14)$$

where γ is the Euler-Mascheroni constant. For large values of U_0, variational calculations [57] show that

$$E_{1s} \underset{U_0 \gg 1}{\simeq} -E_0\left(2U_0 - 4\sqrt{\frac{3U_0}{2}} + \frac{15}{4}\right). \quad (15)$$

We see that these perturbative expressions match well with our numerical results in the two limits, as shown in Fig. 3.

In addition to the $1s$ bound state, we find that the interlayer dipolar potential can bind an increasing number of dimer states with increasing U_0. The corresponding thresholds are indicated as gray vertical lines in Fig. 3 and are listed in Table III. In order of increasing U_0, the sequence of additional dimer states that eventually bind is $2p$, $2s$, $3d$, $3p$, $4f$, $3s$, $4d$, ... Note that this order can change when we introduce the effects of Pauli blocking at finite E_F, even though the orbital angular momentum remains a good quantum number for $Q = 0$.

For each bound state with energy $E_{n\ell} < 0$, we evaluate in Fig. 4 the corresponding dimer eigenfunctions in real space,

$$\eta_{n\ell}(r) = i^\ell \int \frac{k\,dk}{2\pi} J_\ell(kr) \tilde{\eta}_{k\ell}^{(Q=0,n)}, \quad (16)$$

where $J_\ell(x)$ is the Bessel function of the first kind. We find that, at small distances $r \lesssim d$, the dimer wave functions can
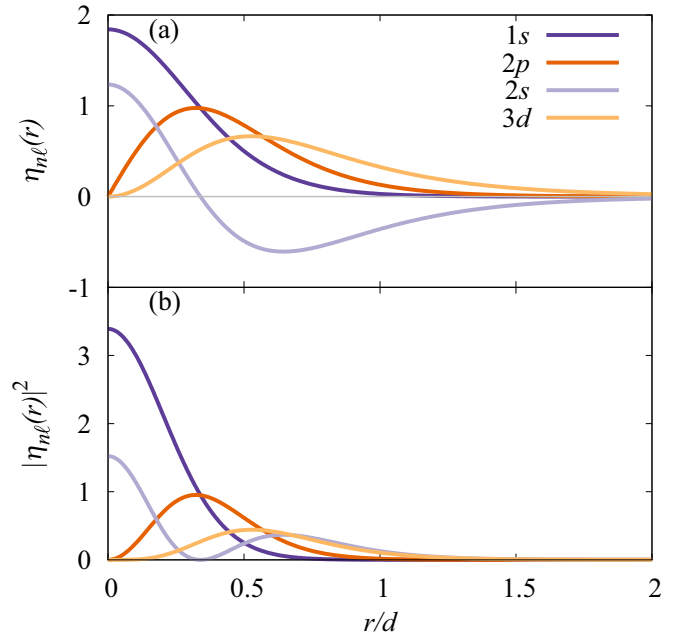

FIG. 4. Real-space dimer wave functions in the case of $E_F = 0$, Eq. (16). We show (a) $\eta_{n\ell}(r)$ and (b) $|\eta_{n\ell}(r)|^2$ for $U_0 = 30$.

be well approximated as

$$\eta_{1s}(r) \simeq \lambda_{1s} e^{-\alpha_{1s} r^2}, \tag{17a}$$

$$\eta_{2s}(r) \simeq \lambda_{2s} e^{-\alpha_{2s} r^2}(1 - \beta_{2s} r), \tag{17b}$$

$$\eta_{2p}(r) \simeq \lambda_{2p} r e^{-\alpha_{2p} r^2}, \tag{17c}$$

$$\eta_{3d}(r) \simeq \lambda_{3d} r^2 e^{-\alpha_{3d} r^2}. \tag{17d}$$

This is similar to the hydrogenic atom in 2D [51], with the difference being that the dipolar potential leads to a stronger confinement to shorter distances than the Coulomb potential, i.e., the wave functions are concentrated at $r < d$.

Apart from the two-body bound states, we might wonder about the scattering properties of the interlayer dipolar potential (2). In particular, one can show [34] that there is only a very restricted parameter regime of scattering energies $E \lesssim E_0$ and values of $U_0 \approx 1$ where the scattering properties of the dipolar potential recover those of a short-range contact-like attractive potential. This, as also discussed in Ref. [34], is due to the fact that for $U_0 < 1$ the potential leads to a very shallow bound $1s$ state, while for $U_0 > 1$ there are additional states becoming bound. We discuss these aspects in Appendix A, where we explicitly evaluate the scattering phase shift within the variable-phase method.

B. Finite-E_F and finite-Q dimers

Similarly to the case of other attractive interaction potentials, the dimer ground state spontaneously acquires a finite center-of-mass momentum $Q_{\min}$ above a threshold density of fermions [45,58–60]. Such a dimer state can be regarded as the extreme imbalance limit of the FFLO phase in spin-imbalanced superconductors [61,62]. Over the last few decades there has been significant interest in studying this inhomogeneous superfluid phase in a variety of physical systems—see, e.g., recent reviews [63,64]. The possibility of generating such a phase has already been studied in Ref. [37] for fermionic dipolar molecules in a bilayer geometry with a finite imbalance of layer densities. Here, it was found that, when the imbalance exceeds a critical value, the system undergoes a transition from a uniform interlayer superfluid phase to the FFLO phase and that this phase is enhanced by the long-range character of the interlayer dipolar interaction. Indeed, it has previously been shown that unscreened Coulomb interactions significantly stabilizes the FFLO phase [58].

In this section, we consider this problem from the perspective of the extremely imbalanced limit, with a single particle in layer 2. We show in Fig. 5 the spontaneous formation of a dimer state with finite center-of-mass momentum for the specific case of $U_0 = 5$. In this case, we observe that the $1s$ dimer state has a minimum at $Q = 0$ for $E_F \lesssim 0.46E_0$. For larger densities of the Fermi sea in layer 1, the lowest energy solution is for $Q = Q_{\min} \neq 0$, with energy $E^{(Q_{\min})} < E^{(Q=0)}$, in which case the orbital angular momentum ceases to be a good quantum number. For the range of E_F studied in this work ($E_F \lesssim 6E_0$), we do not observe any unbinding of the finite-Q dimer state, i.e., we find that the dimer energy remains below the energy E_F of the normal state $|N\rangle = \hat{c}_{\mathbf{0},2}^\dagger \hat{c}_{\mathbf{k}_F,1}^\dagger |\text{FS}\rangle$.

As also commented in Ref. [37], the long-range nature of the dipole-dipole interaction can mix different
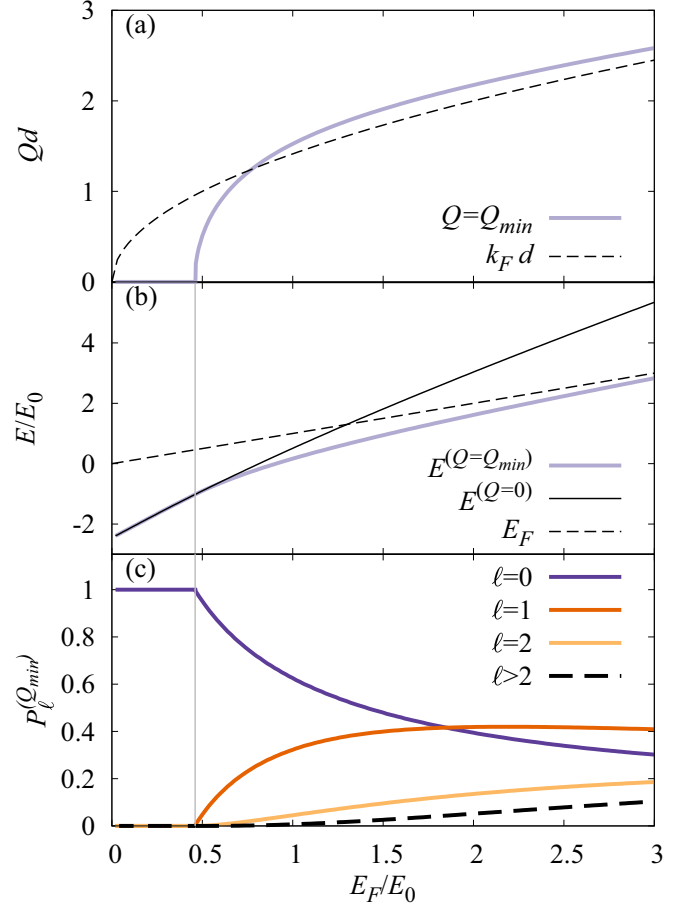

FIG. 5. Spontaneous appearance of a finite dimer center-of-mass momentum when increasing the density of fermions in layer 1 for $U_0 = 5$. (a) Values of the center-of-mass momentum $Q_{\min}$ corresponding to the lowest dimer energy. (b) Dimer ground-state energy for $Q = Q_{\min}$ (purple solid line) and $Q = 0$ (black solid line). The dashed line is the energy of the normal state, E_F. The (gray) vertical line indicates the threshold for $Q_{\min} \neq 0$. (c) Probability (18) that the dimer lowest eigenstate at $Q_{\min}$ contains an orbital angular-momentum component ℓ.

angular-momentum components of the paired state and thus enhance the FFLO regime. We evaluate the probability that the lowest-energy dimer eigenstate contains an orbital angular-momentum component ℓ as

$$P_\ell^{(Q_{\min})} = \int_{k_F}^\infty \frac{k\,dk}{2\pi} \left| \tilde{\eta}_{k\ell}^{(n=1,+,Q_{\min})} \right|^2. \tag{18}$$

We plot $P_\ell^{(Q_{\min})}$ as a function of E_F in Fig. 5(c). When $Q = 0$, the lowest-energy state is $1s$ because ℓ is a good quantum number. However, for $E_F > 0.46E_0$ where the lowest dimer state develops a minimum at $Q_{\min} \neq 0$, the lowest eigenvalue is characterized by several orbital angular-momentum components ℓ. As the transition from $Q = 0$ to finite $Q_{\min}$ is second order, the s component ($\ell = 0$) dominates close to the transition. For larger values of E_F, the dimer state acquires first a p-wave component ($\ell = 1$) and, later, a smaller contribution from the $\ell = 2$, as well as $\ell > 2$ components.

In the following section, we illustrate how the properties of the ground and excited states of the two-body bound dimers affect the polaron properties, including its spectral function.

IV. POLARON

We now analyze the spectral properties of the polaron formed by the dipolar impurity in layer 2 which is dressed by particle-hole excitations of the Fermi sea of dipoles in layer 1. To this end, we employ a variational ansatz [65] describing a polaron with zero center-of-mass momentum, $Q = 0$, as the superposition between the bare impurity weighted by the variational parameter ϕ_0 and a single particle-hole excitation, described by $\phi_{\mathbf{kq}}$:

$$|P_3\rangle = \left(\phi_0 \hat{c}^{\dagger}_{\mathbf{0},2} + \sum_{\mathbf{kq}} \phi_{\mathbf{kq}} \hat{c}^{\dagger}_{\mathbf{q}-\mathbf{k},2} \hat{c}^{\dagger}_{\mathbf{k},1} \hat{c}_{\mathbf{q},1}\right)|\text{FS}\rangle. \quad (19)$$

Here, we use a notation where $\mathbf{k}$ is the momentum of the particle states ($k > k_F$) and $\mathbf{q}$ of the hole states ($q < k_F$). The polaron state is normalized so that $1 = |\phi_0|^2 + \sum_{\mathbf{kq}} |\phi_{\mathbf{kq}}|^2$.

The variational ansatz in Eq. (19) has previously been successfully employed to describe the impurity problem in different contexts, including ultracold atoms [41–45] and doped semiconductors [47–50]. In the case of contact interactions, truncating the dressing of the Fermi sea to a single particle-hole excitation has been demonstrated to be an excellent approximation, with an almost exact cancellation of higher-order contributions [66].

Previous work on the dipolar case [38] employed a T-matrix approach to evaluate the lowest attractive polaron branch energy, but the entire spectrum of excitations and the important role played by excited dimer states have not previously been considered. Furthermore, we find that there are important qualitative differences between the variational ansatz (19) and the T-matrix approach. This is unlike the case of a pure contact interaction, where the variational ansatz in Eq. (19) is completely equivalent to the T-matrix approach within a ladder approximation [67]. This highlights the important role played by the longer-range parts of the dipolar interaction potential, despite the dipole-dipole interaction formally corresponding to a short-range interaction in the sense that one can define an asymptotic region and an associated 2D scattering length [68]. We discuss in Appendix B the precise relation between the ansatz (19) and the T-matrix approach employed in Ref. [38].

By minimizing the expectation value $\langle P_3|(\hat{H} - E)|P_3\rangle$ with respect to the variational parameters ϕ_0 and $\phi_{\mathbf{kq}}$, the polaron spectral properties can be found by solving the eigenvalue problem

$$E\phi_0 = \sum_{\mathbf{k},\mathbf{q}} V_{|\mathbf{k}-\mathbf{q}|}\phi_{\mathbf{kq}}, \quad (20a)$$

$$E\phi_{\mathbf{kq}} = E_{\mathbf{kq}}\phi_{\mathbf{kq}} + V_{|\mathbf{k}-\mathbf{q}|}\phi_0$$
$$+ \sum_{\mathbf{k}'} V_{|\mathbf{k}-\mathbf{k}'|}\phi_{\mathbf{k}'\mathbf{q}} - \sum_{\mathbf{q}'} V_{|\mathbf{q}-\mathbf{q}'|}\phi_{\mathbf{kq}'}, \quad (20b)$$

where $E_{\mathbf{kq}} = \epsilon_{\mathbf{k}} - \epsilon_{\mathbf{q}} + \epsilon_{\mathbf{q}-\mathbf{k}}$ and where we have omitted the terms that are zero because $V_{\mathbf{0}} = 0$. The polaron spectral

function $A(\omega)$ can be evaluated as usual from the impurity Green's function $G(\omega)$ [69]:

$$G(\omega) = \sum_n \frac{|\phi_0^{(n)}|^2}{\omega - E^{(n)} + i\eta}, \quad (21a)$$

$$A(\omega) = -\frac{1}{\pi}\text{Im}G(\omega). \quad (21b)$$

Similarly to the dimer problem, it is profitable to project the eigenvalue problem (20) onto an eigenbasis of the orbital angular momentum. This simplifies the numerical solution considerably, because we see that the polaron branches are characterized by a small number of partial waves ℓ. Thus, we consider the following Fourier series of the dimer-hole wave functions:

$$\phi_{kq\varphi} = \sum_{\ell \in \mathbb{Z}} e^{i\ell\varphi}\tilde{\phi}_{kq\ell}.$$

The eigenvalue equations (20) now read

$$E\phi_0 = \int \frac{k\,dk}{2\pi}\frac{q\,dq}{2\pi}\sum_{\ell \in \mathbb{Z}} \tilde{V}(k,q,\ell)\tilde{\phi}_{kq\ell}, \quad (22a)$$

$$E\tilde{\phi}_{kq\ell} = 2\epsilon_{\mathbf{k}}\tilde{\phi}_{kq\ell} - \frac{kq}{2m}(\tilde{\phi}_{kq\ell-1} + \tilde{\phi}_{kq\ell+1})$$
$$+ \tilde{V}(k,q,\ell)\phi_0 + \int \frac{k'dk'}{2\pi}\tilde{V}(k,k',\ell)\tilde{\phi}_{k'q\ell}$$
$$- \int \frac{q'dq'}{2\pi}\tilde{V}(q,q',\ell)\tilde{\phi}_{kq'\ell}, \quad (22b)$$

where we have employed Eq. (11). As for the dimer wave function, it is convenient to introduce symmetric and antisymmetric solutions for the exchange $\ell \mapsto -\ell$:

$$\tilde{\phi}^{(\pm)}_{kq\ell} = \frac{\tilde{\phi}_{kq\ell} \pm \tilde{\phi}_{kq,-\ell}}{2}, \quad (23)$$

where $\tilde{\phi}^{(+)}_{kq0} = \tilde{\phi}_{kq0}$ and $\tilde{\phi}^{(-)}_{kq0} = 0$. Restricting to $\ell \geqslant 0$, the eigenvalue equations become

$$E\phi_0 = \int \frac{k\,dk}{2\pi}\frac{q\,dq}{2\pi}\sum_{\ell \geqslant 0}(2 - \delta_{\ell,0})\tilde{V}(k,q,\ell)\tilde{\phi}^{(+)}_{kq\ell}, \quad (24a)$$

$$E\tilde{\phi}^{(\pm)}_{kq\ell} = 2\epsilon_{\mathbf{k}}\tilde{\phi}^{(\pm)}_{kq\ell} - \frac{kq}{2m}(\tilde{\phi}^{(\pm)}_{kq|\ell-1|} + \tilde{\phi}^{(\pm)}_{kq\ell+1})$$
$$+ \delta_{\pm,+}\tilde{V}(k,q,\ell)\phi_0 + \int \frac{dk'k'}{2\pi}V(k,k',\ell)\phi^{(\pm)}_{k'q\ell}$$
$$- \int \frac{dq'q'}{2\pi}V(q,q',\ell)\phi^{(\pm)}_{kq'\ell}. \quad (24b)$$

We thus find that the equations for symmetric and antisymmetric dimer-hole wave functions decouple. Most importantly, the impurity wave function ϕ_0 only couples to the symmetric dimer-hole wave function $\tilde{\phi}^{(+)}_{kq\ell}$. Thus, the antisymmetric solutions will lead to additional eigenvalues for the polaron problem but these will all have zero spectral weight. As such, we can halve the degrees of freedom in the problem by neglecting the antisymmetric sector.
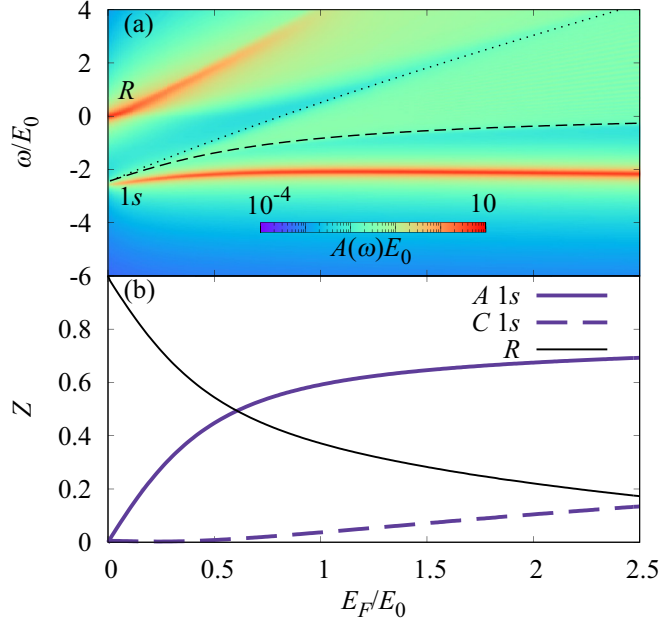
FIG. 6. Polaron spectral properties for $U_0 = 5$. (a) Spectral function $A(\omega)$ as a function of E_F and energy. The (black) dashed and dotted lines are the boundaries of the dimer-hole continuum (see text). The broadening has been fixed to $\eta = 0.05E_0$. (b) Evolution of the polaron spectral weights Z as a function of E_F for the attractive (A) $1s$ branch, its continuum (C), and the repulsive (R) branch.

By discretizing the eigenvalue equations on a Gauss-Legendre grid in $k \in (k_F, \infty)$ and $q \in (0, k_F)$ and including a finite number of values ℓ, we numerically diagonalize Eq. (24) to find eigenvalues and eigenvectors and thus evaluate the polaron spectral function according to Eq. (21). We have checked that all our results are numerically converged with respect to the number of points in the momentum grids as well as in the number of ℓ values. It is interesting to note that when $\omega < 0$ we need only very few, around four, values of ℓ to obtain converged results in the considered parameter regime, while to describe the scattering states we find that nine values of ℓ are sufficient.

A. Spectral properties

We now analyze the properties of the polaron spectral function for increasing values of U_0. We see that there are strong qualitative differences between the spectra, which originate from the different numbers and types of dimer bound states. We now go through these in detail.

Let us first discuss the case $U_0 = 5$, corresponding to Fig. 6, for which only the $1s$ two-body dimer state is bound (see Fig. 3). The spectrum in Fig. 6(a) is characterized by two polaron branches and a continuum of states. For $\omega < 0$, the attractive polaron branch recovers the energy of the $1s$ dimer state in the limit $E_F \to 0$, and we thus label it as the $1s$ attractive branch. This resonance is well separated from the continuum, and its energy coincides with the lowest energy-eigenvalue of Eq. (24). The polaron spectrum also exhibits another resonance at $\omega \gtrsim 0$, the repulsive polaron, which corresponds to a continuum of states rather than being
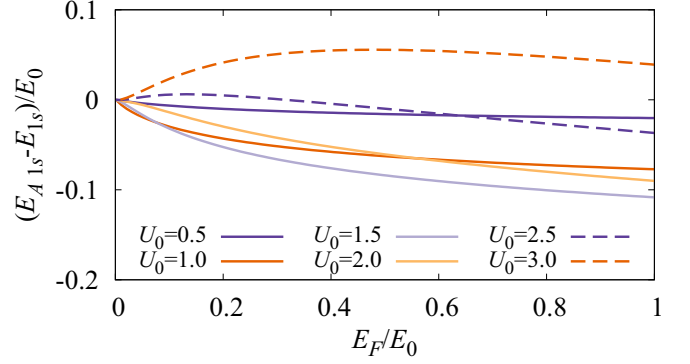

FIG. 7. Energy of the $1s$ attractive branch measured from the ground-state energy of the vacuum dimer state, E_{1s}, as a function of E_F for different values of U_0.

characterized by a single eigenvalue. When $E_F \to 0$, the repulsive polaron recovers the energy of the bare impurity at rest, $\omega = 0$, while it blueshifts when E_F increases. Simultaneously, it broadens and loses spectral weight. In between the attractive and repulsive branches is a continuum of states where the hole in the $\hat{c}^\dagger_{\mathbf{q}-\mathbf{k},2} \hat{c}^\dagger_{\mathbf{k},1} \hat{c}_{\mathbf{q},1}$ complex of the polaron state (19) is unbound, while the dimer is bound. The energy of such a state is that of a dimer with center-of-mass momentum $\mathbf{q}$ and a hole at momentum $\mathbf{q}$, and hence the boundaries of this dimer-hole continuum are $E^{(q=0)}$ and $E^{(q=k_F)} - E_F$, respectively, where the energy is computed using Eq. (12).[4] Both energies recover E_{1s} when $E_F \to 0$, as expected.

A distinctive feature of the spectrum in Fig. 6(a) is that the $1s$ attractive branch blueshifts (increases its energy) as we increase E_F. This is in contrast with the case of contact interactions [43,44] where the attractive branch always redshifts (lowers its energy) with increasing E_F. The origin of this qualitatively new feature is that the dipole-dipole scattering can be significant at low momenta [see Fig. 2(b)] and therefore the hole scattering can be strongly enhanced relative to particle scattering despite the reduced phase space. As also discussed in Appendix B, we can specifically trace the difference to the term $-\sum_{\mathbf{q}'} V_{|\mathbf{q}-\mathbf{q}'|} \phi_{\mathbf{k}\mathbf{q}'}$ in Eq. (20), which is not present in the previous T-matrix treatment of the dipolar polaron problem [38]. This term is negligible for $U_0 \lesssim 2$, in which case the $1s$ attractive branch redshifts when E_F increases, but it becomes important for larger values of U_0. The change from redshift to blueshift with increasing U_0 is shown in Fig. 7, where we plot the evolution with E_F of the energy of the $1s$ attractive branch measured from the vacuum dimer energy E_{1s}.

Figure 6(b) shows the spectral weight Z for each of the branches, which is defined as the area of the spectral function under the corresponding peak. Because the eigenvectors of the polaron problem form a complete basis, the spectral function satisfies the sum rule $\int_{-\infty}^\infty d\omega A(\omega) = 1$, and thus the total

---

[4]Note that we only plot the dimer energy at finite center of mass $E^{(q=k_F)}$ corresponding to the symmetric states under the exchange $\ell \mapsto -\ell$ in Eq. (12) since these are the only ones with finite spectral weight. Instead, for zero center-of-mass momentum, the symmetric and antisymmetric solutions are degenerate in energy.
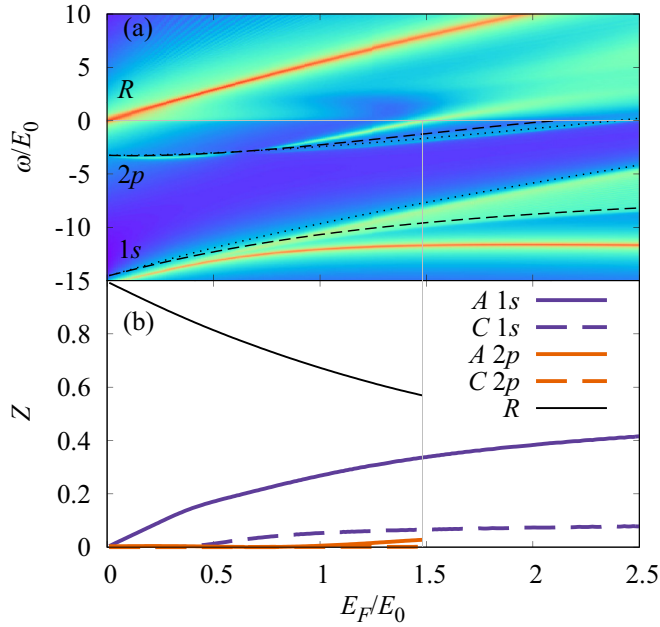
FIG. 8. Polaron spectral properties for $U_0 = 15$. (a) Dipolar Fermi polaron spectrum as a function of E_F and energy. The (black) dashed and dotted lines are the boundaries of the $1s$ and $2p$ dimer-hole continua (see text). The broadening has been fixed to $\eta = 0.05E_0$. (b) Evolution of the polaron spectral weights Z as a function of E_F for the attractive (A) $1s$ and $2p$ branches, their continua (C), and the polaron repulsive (R) branch. The vertical gray line indicates when the A $2p$ branch enters into the continuum at $\omega = 0$.

spectral weight is always one for all interaction strengths and densities. When $E_F \approx 0$, the spectral weight belongs entirely to the repulsive polaron branch, which coincides with the noninteracting impurity. When E_F increases, we see that Z is transferred mostly to the attractive branch, first linearly and then sublinearly. Only a small part of the spectral weight is transferred to the dimer-hole continuum.

In Fig. 8 we show the case of stronger interactions $U_0 = 15$ at which also the dimer state $2p$ is bound (see Fig. 3). Now, the impurity spectrum changes qualitatively from the previous case because there are two attractive polaron branches: when $E_F \to 0$, one recovers, as before, the energy of the $1s$ dimer state, E_{1s}, while the second branch recovers the energy of the $2p$ dimer state, E_{2p}. Here, we label the attractive polaron resonances by $1s$ and $2p$ even though their orbital angular-momentum components evolve with E_F and change in character (see below). Both attractive resonances have an associated dimer-hole continuum: as before, the boundaries of these are the energies of the dimer states $E^{(q=0)}$ and $E^{(q=k_F)} - E_F$.[5] While the $1s$ dimer-hole continuum is higher in energy than the $1s$ attractive branch, we find that this is not necessarily the case for the $2p$ branch, which for $E_F \gtrsim E_0$ clearly appears above its dimer-hole continuum (for $E_F < E_0$, the spectral weight is very small and it is difficult to distinguish it from its dimer-hole continuum). Both the $2p$ attractive

---

[5]Note that only for the $1s$ state do we always have $E^{(q=k_F)} - E_F < E^{(q=0)}$.

branch and the continuum blueshift in energy for increasing E_F and, eventually, move into the continuum of the $q = 0$ dimer state at $\omega = 0$.

Figure 8(a) also shows how the spectral weight of the repulsive branch is predominantly transferred to the s-wave-like attractive branch and how, compared with the case of $U_0 = 5$ in Fig. 6, the spectral weight is transferred more slowly because the $1s$ state is deeper bound. As a result, the repulsive branch remains brighter and broadens more slowly for increasing E_F than in the previous case. This is further analyzed in Fig. 8(b), where we see that the $1s$ attractive branch spectral weight grows linearly with E_F for small E_F, while the $2p$ attractive branch spectral weight grows sublinearly and remains very small. Note that, with increasing density, the $2p$ attractive branch enters the continuum (vertical gray line in Fig. 8), in which case the criterion that we employ to evaluate the spectral weight of both the attractive and repulsive branches becomes inapplicable due to the rapid broadening of both modes. In Fig. 8(b), we thus stop plotting their spectral weights at this point.

To gain further insight into the angular-momentum structure of the polarons, we can evaluate the probability that the hole in a given dimer-hole eigenstate n has an orbital angular-momentum component ℓ [49]:

$$P_\ell^{(n)} = \frac{1}{1 - |\phi_0|^2} \int \frac{k\,dk}{2\pi} \frac{q\,dq}{2\pi} |\tilde{\phi}_{kq\ell}^{(+,n)}|^2. \qquad (25)$$

Because only the symmetric $+$ states (23) have a finite spectral weight, the probability satisfies $P_{-\ell}^{(n)} = P_\ell^{(n)}$. Furthermore, the probability is normalized such that $\sum_{\ell \geqslant 0} P_\ell^{(n)} = 1$. In Fig. 9, we plot the polaron spectral function for $U_0 = 15$ for different values of E_F together with the probability $P_\ell^{(n)}$ for $\ell = 0, 1, 2$ as a function of ω (with the dots corresponding to discrete eigenvalues). One can clearly see that, for $E_F < E_0$, the eigenvalues n corresponding to the $1s$ attractive branch and its continuum are predominantly s wave, i.e., $P_0^{(n)} \approx 1$, while $P_{\ell > 0}^{(n)} \approx 0$, and the eigenvalues n corresponding to the $2p$ attractive branch and its continuum are predominantly p wave, i.e., $P_1^{(n)} \approx 1$, while $P_{\ell \neq 1}^{(n)} \approx 0$. However, for larger values of E_F, there is an evolution of these probabilities, where the $1s$ branch acquires a p-wave component, while the $2p$ branch acquires both s- and d-wave components. As far as the dimer-hole continuum is concerned, as already discussed in Sec. III, the dimer state at zero center of mass corresponds to a single value of the orbital angular momentum ℓ. This can be clearly seen in Fig. 9, where we recognize the energies of the dimer at zero center of mass $E^{(q=0)}$ limiting the dimer-hole continua, as those having $P_\ell^n = 1$, with either $\ell = 0$ or $\ell = 1$. However, for the other boundary of the dimer-hole continua, $E^{(q=k_F)} - E_F$, the dimer state at finite center-of-mass momentum is generally not an eigenstate of the orbital angular momentum and involves a mixture of ℓ values that evolve with E_F.

In Fig. 10 we plot the spectrum for strong dipolar interactions, $U_0 = 24$, for which also the $2s$ dimer state becomes bound. Here, the repulsive branch very quickly transfers its spectral weight to the nearby $2s$ attractive branch—see Fig. 10(b). The behavior of the $2p$ attractive branch is very similar to the case $U_0 = 15$ analyzed previously. On the other hand, the $1s$ attractive branch now becomes deeply bound and,
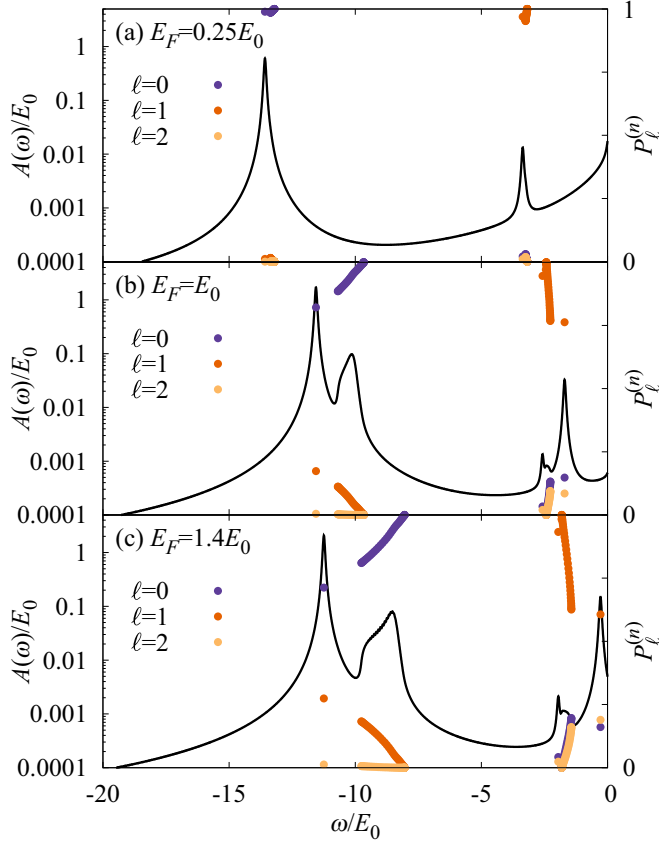
FIG. 9. Polaron spectral function as a function of energy for three different values of the Fermi energy E_F and for $U_0 = 15$. Symbols (values on the right y axis) are the probabilities $P_\ell^{(n)}$ that the dimer polaron component has a value of the orbital angular momentum equal to $\ell = 0, 1, 2$ for a given eigenvalue n (24).

differently from before, it is the associated dimer-hole continuum that gains spectral weight first, with the 1s attractive branch only overcoming the spectral weight of the dimer-hole continuum for $E_F \gtrsim E_0$.

The strong distinction between the growth rate of the 1s state in the presence and absence of the 2s state leads us to define the spectral weight growth rate at small E_F, $\alpha = dZ/d(E_F/E_0)|_{E_F=0}$. We show the results for the 1s and 2s attractive branches in Fig. 11 as a function of U_0. While for $U_0 < 17.8$, the 1s attractive branch spectral weight grows linearly with E_F, when the 2s attractive branch appears for $U_0 > 17.8$, the 1s attractive branch spectral weight grows sublinearly and it is instead the spectral weight of its continuum that grows linearly with E_F.

In Fig. 12, we plot the evolution of the probability $P_\ell^{(n)}$ defined in Eq. (25) as a function of E_F for those eigenvalues n that correspond to the 1s, 2p, and 2s attractive branches, for the three different values of U_0 that correspond to Figs. 6, 8, and 10, respectively. We see that the 1s attractive branch orbital character is predominantly s wave at low density, as expected, before becoming more p wave with increasing E_F. However, for the attractive 2p branch, even though the p-wave character dominates over the entire E_F interval studied, there is an exchange with both s- and d-wave components
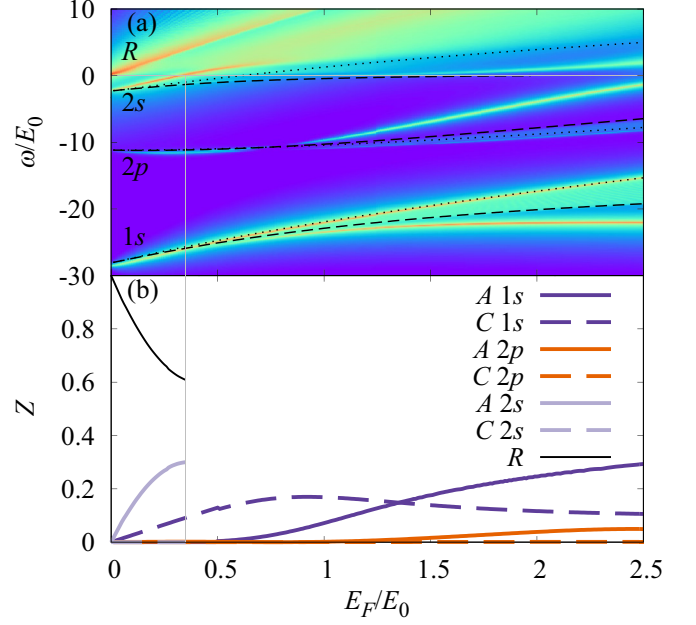

FIG. 10. Polaron spectral properties for $U_0 = 24$. (a) Dipolar Fermi polaron spectrum as a function of E_F and energy. The (black) dashed and dotted lines are the boundaries of the 1s, 2p, and 2s dimer-hole continua (see text). The broadening has been fixed to $\eta = 0.05E_0$. (b) Evolution of the polaron spectral weights Z as a function of E_F for the attractive (A) 1s, 2p, and 2s branches, their continua (C), and the polaron repulsive (R) branch. The vertical gray line indicates when the A 2s branch enters into the continuum at $\omega = 0$.

when E_F increases. Finally, the 2s attractive branch quickly loses its s-wave character towards both the p- and d-wave components, before merging with the continuum at $\omega > 0$. We can in general see that, as U_0 increases, the exchange of angular-momentum components is slower due to the attractive branches moving further apart in energy.

Finally, we note that an alternative way of presenting the polaron spectral properties is one where energy scales are rescaled by E_F and length scales by $1/k_F$. In this case, we fix
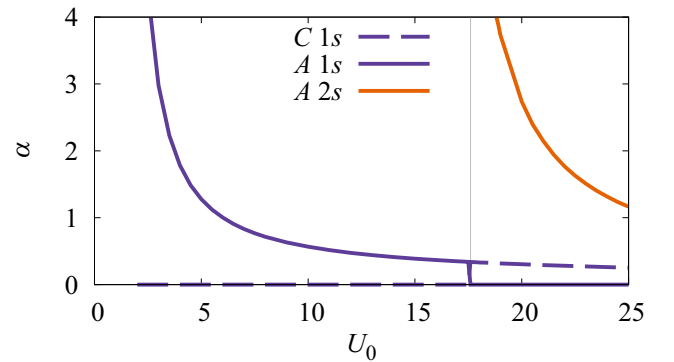

FIG. 11. Growth rate of the spectral weight at small densities $\alpha = dZ/d(E_F/E_0)_{E_F=0}$ of the 1s and 2s attractive (A) branches and of the 1s continuum (C) as a function of the dipolar interaction strength U_0. The (gray) vertical lines indicates the binding threshold for the 2s state $U_{02s} \simeq 17.8$ (see Fig. 3).
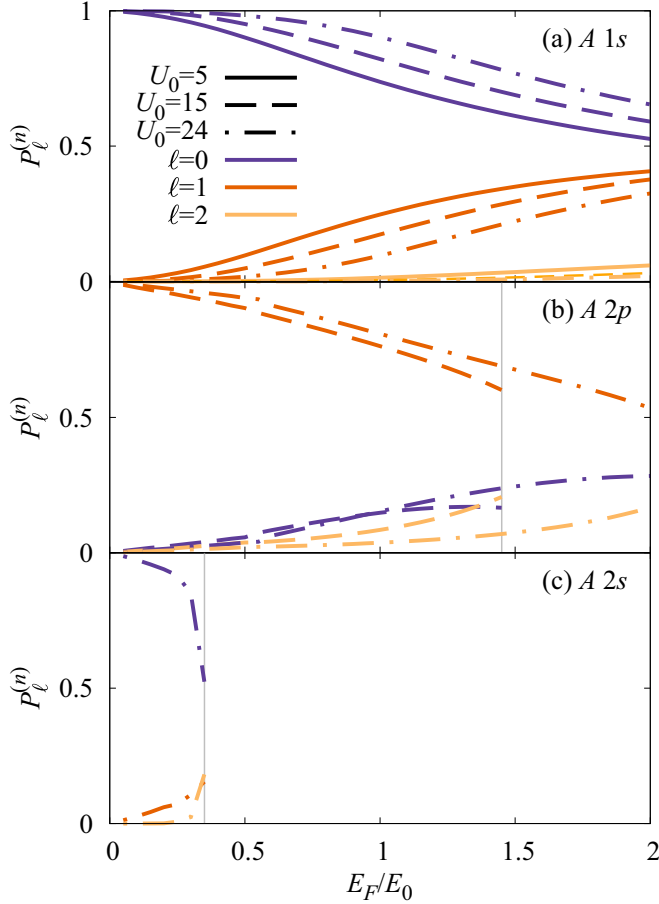
FIG. 12. Probability $P_\ell^{(n)}$ that the dimer polaron component has a value of the orbital angular momentum equal to $\ell = 0, 1, 2$ for those eigenvalue indices n corresponding to the attractive (a) 1s, (b) 2p, and (c) 2s branches. The vertical (gray) line in panel (b) indicates when the A 2p branch enters the continuum for $U_0 = 15$ (see Fig. 8), and the one in panel (c) when the A 2s branch enters the continuum for $U_0 = 24$ (see Fig. 10).

the dipolar interaction parameter U_F (6) and study the polaron spectrum by varying an additional dimensionless parameter, such as E_0/E_F or $1/k_F d$:

$$\frac{1}{k_F d} = \sqrt{\frac{E_0}{2E_F}} = \frac{U_0}{U_F}.$$

We plot in Fig. 13 the impurity spectral function obtained by fixing U_F and increasing $1/k_F d$. In the units previously employed, this corresponds to simultaneously increasing U_0 and decreasing E_F/E_0, which we see leads to the binding of an increasing number of dimer states. As shown in Fig. 13(a), the branches with stronger spectral weight are those associated with the s-wave dimer states. In Figs. 13(b)–13(d) we plot the spectral function at a fixed value of energy $\omega < 0$ as a function of $1/k_F d$. As a color map, we plot the fraction of the spectral function with angular momentum ℓ, defined as the ratio between the angular-momentum weighted
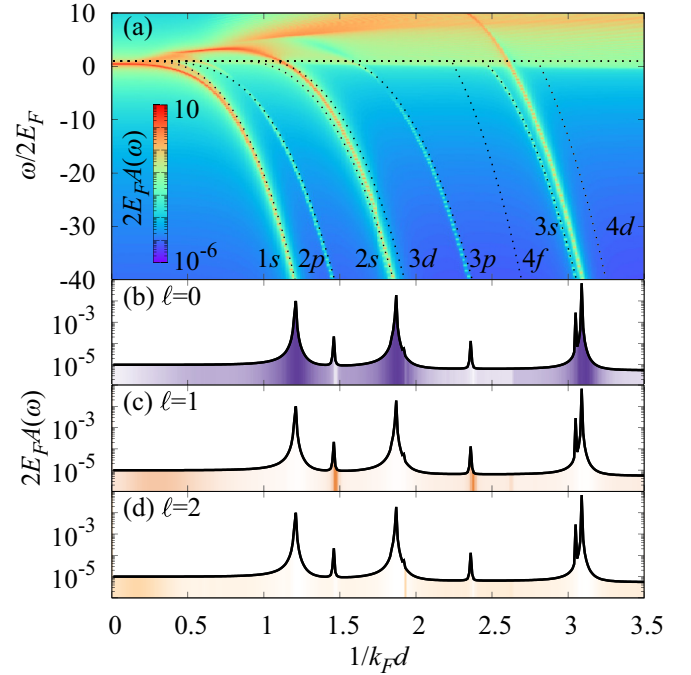

FIG. 13. Polaron spectral properties for $U_F = 15\sqrt{2}$. (a) Dipolar Fermi polaron spectrum as a function of $1/k_F d$ and energy. The (black) dotted lines are the dimer energies at zero momentum, $E^{(q=0)}$, from the 1s state up to the 4d one—unbinding of the zero-momentum dimer occurs at $\omega = 2E_F$ (horizontal dotted line). The broadening has been fixed to $\eta = 0.05 \times 2E_F$. Panels (b)–(d) are the spectral functions at $\omega = -40 \times 2E_F$ as a function of $1/k_F d$ and the color maps are the fractions of the spectral function with angular momentum ℓ, $A_\ell(\omega)/A(\omega)$ (26) for $\ell = 0, 1, 2$.

spectral function:

$$A_\ell(\omega) = -\frac{1}{\pi} \text{Im}\left[\sum_n \frac{P_\ell^{(n)} |\phi_0^{(n)}|^2}{\omega - E^{(n)} + i\eta} \right], \qquad (26)$$

and $A(\omega)$—note that $\sum_{\ell \geqslant 0} A_\ell(\omega) = A(\omega)$. This allows us to identify the dominant orbital angular-momentum component ℓ of each attractive branch, which we see is strongly correlated with the angular momentum of the corresponding bound dimer state.

Making use of these units, we compare in Fig. 14 the results for the energy of the 1s attractive branch obtained within the polaron ansatz (19) with those obtained in Ref. [39] by quantum Monte Carlo (QMC) methods for different values of U_F. For $U_F = 0.5$, there is excellent agreement between the two theories for any value of $k_F d$, suggesting that, within this regime, disregarding intralayer interactions is a reliable approximation. For larger values of U_F, perfect agreement is observed only at small $k_F d$ values, where the polaron energy closely matches that of the vacuum dimer state. For increasing $k_F d$ values, where layer 1 approaches the transition to a broken-symmetry phase [28,29], we find that deviations increase, although the qualitative behavior remains similar.
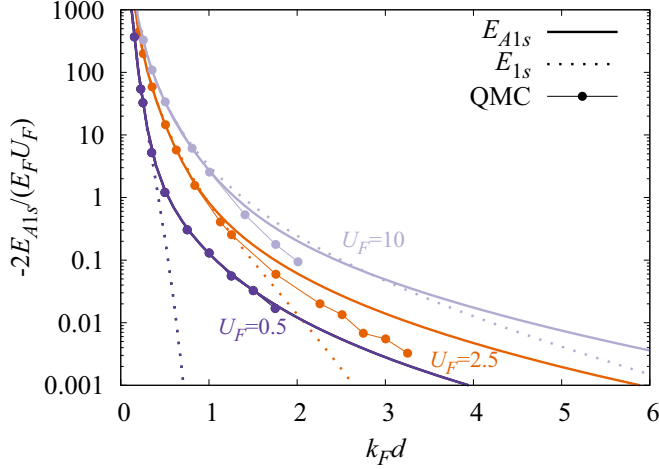
FIG. 14. Energy of the 1s attractive branch evaluated as a function of $k_F d$ for different values of U_F (solid lines). We compare our results with those obtained in Ref. [39] by QMC methods (symbols) and with the energy of the vacuum dimer state E_{1s} (dotted lines).

V. TUNNELING RATE AND IMPURITY SPECTRAL FUNCTION

We now discuss how one can experimentally probe the spectral function. Our proposal is inspired by radio-frequency spectroscopy [70], where one can inject (eject) the impurity by driving transitions from (to) an auxiliary hyperfine state that, in the ideal case, does not interact with the medium. Similarly, we suggest to use an auxiliary layer ($\sigma = 3$) that the impurity can tunnel into or from—see Fig. 15. We furthermore assume that interactions between the dipolar particles can occur only between layers 1 and 2, while tunneling can only occur between layers 2 and 3. This situation can, e.g., be achieved if a potential barrier is present between layers 1 and 2, while layer 3 is further away from both layers. We also note that, in practice, a small 1-3 interaction can be taken into account by considering the initial state to be a weakly dressed attractive polaron, similarly to what is routinely done in the case of rf spectroscopy for contact interactions, see, e.g., Ref. [71].

We thus have to extend the Hamiltonian (1) to include two additional terms, $\hat{H}_3$ and $\hat{H}_t$, that describe, respectively, the kinetic energy of the particles in layer 3, and the tunneling between layers 2 and 3:

$$\hat{H}_3 = \sum_{\mathbf{k}} (\epsilon_{\mathbf{k}} + \Delta)\hat{c}^\dagger_{\mathbf{k},3}\hat{c}_{\mathbf{k},3}, \tag{27a}$$

$$\hat{H}_t = t \sum_{\mathbf{k}} \hat{c}^\dagger_{\mathbf{k},3}\hat{c}_{\mathbf{k},2} + \text{H.c.} \tag{27b}$$

Note that in the kinetic term $\hat{H}_3$ we have included a "detuning" energy Δ, which represents the difference between the energy minima of the confining potentials in the z direction.

The additional terms in the Hamiltonian exactly match those used in radio-frequency spectroscopy on impurities [72], where Δ plays the role of the radio-frequency detuning, and t the role of the Rabi coupling. Therefore, this auxiliary layer provides access to the spectral properties. To be specific, within linear response the tunneling rate can be evaluated using Fermi's golden rule between an initial state consisting
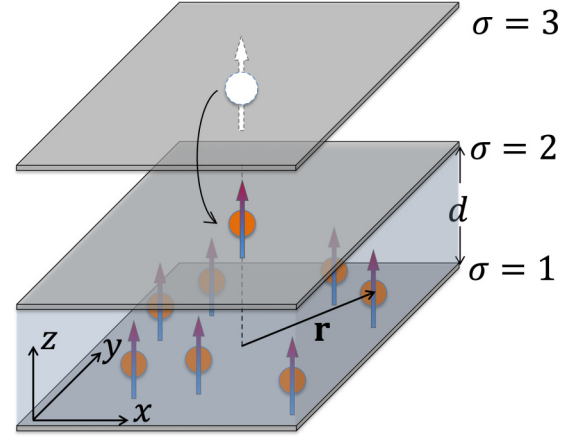

FIG. 15. Illustration of how the impurity spectral function can be probed via tunneling from an auxiliary distant layer $\sigma = 3$ to the impurity layer $\sigma = 2$. Tunneling is suppressed between layers 1 and 2 by a barrier (blue filled region).

of one particle in layer 3 plus a Fermi sea of dipoles in layer 1, $\hat{c}^\dagger_{\mathbf{0},3}|\text{FS}\rangle$, while the final state is the polaron state $|P_3\rangle$ (19). This gives

$$\Gamma_{3\mapsto 2}(\Delta) = 2\pi t^2 \sum_n \left|\langle P_3^{(n)}|\hat{c}^\dagger_{\mathbf{0},2}|\text{FS}\rangle\right|^2 \delta(\Delta - E^{(n)})$$

$$= -2\pi t^2 \frac{1}{\pi}\text{Im}G(\Delta) = 2\pi t^2 A(\Delta). \tag{28}$$

Thus, measuring the tunneling rate as a function of the energy difference Δ between the two lowest eigenenergies of the z-confining lattice potentials is equivalent to measuring the polaron spectral function $A(\omega)$ (21b) evaluated in this work.

VI. CONCLUSIONS AND PERSPECTIVES

In this work we have studied a gas of dipolar fermions in a bilayer geometry in the limit of extreme imbalance, i.e., a single dipole in one layer interacting with a Fermi sea of dipoles in a different layer. We analyze two different yet connected solutions of this problem. We first investigate the properties of the interlayer dimer bound state, generalized to include the Pauli blocking effect from the inert Fermi sea. We find a series of bound states, characterized by the orbital angular momentum and the principal quantum number, binding for increasing dipolar interaction strength or decreasing bilayer distance. For the dimer ground state, we determine the spontaneous emergence of a finite center-of-mass momentum when increasing E_F above a threshold value. The finite momentum dimer corresponds to the large imbalance limit of the FFLO state studied in Ref. [37]. We find that this state has a mixed partial-wave character, including s-, p-, and d-wave contributions.

The other solution we analyze is the many-body polaron state, where the presence of the impurity in one layer leads to particle-hole excitations of the Fermi sea in the other layer. We derive the polaron spectral properties by employing a single particle-hole variational ansatz, and we propose that the tunneling rate of the impurity from an additional auxiliary layer can be employed to experimentally access the

spectrum. We find that the polaron spectrum is characterized by a series of attractive polaron branches which we trace back to the dimer bound states. At small E_F, the polaron energies and their orbital character recover those of the dimer states. However, both energies and orbital angular-momentum components evolve and interchange with E_F. We find that the energy of the ground-state 1s polaron branch evolves with E_F in a qualitative different way depending on the value of U_0. We explain this distinctive property of finite-range dipole-dipole interactions in terms of whether hole scattering is negligible or not in the polaron formation. We characterize the transfer of oscillator strength from the repulsive branch to the series of attractive branches in terms of their partial-wave character and their distance in energy from the repulsive branch.

In our model, we neglect the repulsive interactions between particles in the Fermi sea. As such, we neglect the possibility of strong intralayer correlations that could lead, at very low temperatures, to the spontaneous appearance of density modulated phases such as stripes [28] and Wigner crystals [29], which are predicted to occur for either strong enough dipolar interactions or large enough Fermi densities. While beyond the scope of our study, an exciting perspective of our work is the generalization of the polaron formalism to include the possibility of the impurity interacting with such strongly correlated phases [39], which could potentially leave signatures in the polaron spectral response. Indeed, this would mirror very recent experiments on exciton polarons in doped 2D semiconductor monolayers which have probed strongly correlated states of 2D electron gases, such as Wigner crystals [73,74], fractional quantum Hall states in proximal graphene layers [75] and correlated-Mott states of electrons in a moiré superlattice [76].

Another interesting perspective of our work would involve considering a configuration where the alignment of the dipoles is tilted at a slight angle relative to the normal direction. In this case, the anisotropy induced by the dipole-dipole interaction results in a distorted Fermi surface [25,26], consequently influencing the properties of the Fermi polaron and giving rise to spatial anisotropies, as illustrated in a three-dimensional setup by Ref. [77]. Indeed, deformations of the Fermi surface have already been experimentally observed in a three-dimensional degenerate dipolar Fermi gas composed of Er atoms [78]. Furthermore, a tilted configuration is expected to stabilize the FFLO state (see, e.g., Ref. [79]) since it breaks the continuous rotational symmetry and thus suppresses the pairing fluctuations that destroy FFLO long-range order [80].

The research data underpinning this publication can be accessed through Ref. [81].

APPENDIX A: SCATTERING PHASE SHIFT

In this Appendix we evaluate the s-wave energy-dependent scattering phase shift $\delta_0(k)$, where $E = k^2/2\mu = k^2/m$, with $\mu = m/2$ being the reduced mass. We use the variable-phase method [82] which allows us to evaluate the phase shift produced by a potential that vanishes for all $r > R$, i.e., we define $V_R(r) = V(r)\Theta(R - r)$. In this sense, the phase shift $\delta_\ell(R)$ can be viewed as the accumulated phase shift at position R in the true potential $V(r)$. In 2D, $\delta_\ell(R)$ satisfies the following first-order, nonlinear differential equation [83]:

$$\frac{d\delta_\ell(R)}{dR} = -\frac{\pi}{2} 2\mu V(R)R[J_\ell(kR)\cos\delta_\ell(R) - Y_\ell(kR)\sin\delta_\ell(R)]^2, \tag{A1}$$

with boundary condition $\delta_\ell(0) = 0$. In this expression, $J_\ell(x)$ and $Y_\ell(x)$ are Bessel functions of the first and second kinds, respectively (the latter are also called Neumann functions), and ℓ is again the orbital angular momentum. Thus, for s wave, $\ell = 0$. Finally, the scattering phase shift in the true potential $V(r)$ is given by the limit $\delta_\ell(k) = \lim_{R\to\infty} \delta_\ell(R)$, and it is a function of the scattering energy through the momentum k in Eq. (A1).

The scattering phase shift for the interlayer dipolar potential (2a) has been previously evaluated in Ref. [34], where the following approximate analytical expression for the s-wave scattering phase shift was obtained for small values of U_0:

$$\tan\delta_0(k) \simeq \frac{-\frac{\pi}{2}I_{JJ}(k) - \frac{\pi^2}{4}[I_{JJJY}(k) - I_{JYJJ}(k)]}{1 - \frac{\pi}{2}I_{JY}(k) - \frac{\pi^2}{4}\left[I_{JJYY}(k) - \frac{1}{2}I_{JY}^2(k)\right]}, \tag{A2}$$

where $J \mapsto J_0(x)$, $Y \mapsto Y_0(x)$, and

$$I_{FG}(k) = \int_0^\infty dr\, rV(r)F(kr)G(kr),$$

$$I_{FGPQ}(k) = \int_0^\infty dr\, rV(r)F(kr)G(kr)$$
$$\times \int_r^\infty ds\, sV(s)P(ks)Q(ks).$$

Using Eq. (14), a small-k expansion of this expression allows us to recover the universal low-energy expression of the phase shift for a short-range potential with a dimer state with binding energy $|E_{1s}|$:

$$\cot\delta_0(k) = \frac{1}{\pi}\ln\left(\frac{k^2/2\mu}{|E_{1s}|}\right). \tag{A3}$$

We note that this is the true phase shift for a contact potential; however other potentials will generally have corrections of $O(k^2)$ [84].

In Fig. 16 we compare the numerical results for the scattering phase shift obtained by solving Eq. (A1) with the approximation (A2) derived in Ref. [34] and the universal low-energy expression in Eq. (A3). While we see that Eq. (A2) is a good approximation for values of $U_0 \lesssim 2$, the phase shift
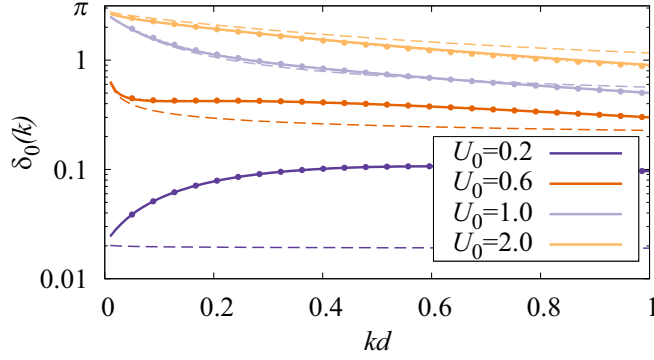
FIG. 16. Phase shift $\delta_0(k)$ as a function of momentum for different values of U_0. Numerical solutions obtained with the variable-phase method (solid) are compared with the analytical expression (A2) derived in Ref. [34] (symbols) and the universal low-energy expression (A3) (dashed).

for a contact potential is a good approximation only when $kd \lesssim 1$ and $U_0 \approx 1$. For $U_0 < 0.6$, as also argued by Ref. [34], the binding energy of the $1s$ state becomes anomalously small and thus the expression (A3) cannot, in practice, be considered the leading term for the low-energy scattering. However, when $U_0 \gtrsim 2$, both approximations become increasingly inaccurate since then there are other dimer states that are close to becoming bound.

APPENDIX B: RELATION BETWEEN T-MATRIX APPROACH AND THE VARIATIONAL ANSATZ

We now discuss the relationship between the T-matrix approach used to obtain the lowest energy attractive polaron branch in Ref. [38] and the variational ansatz (19) that we employ in this work.

For a finite-range scattering potential $V_\mathbf{p}$, the T matrix describes the scattering between an incoming impurity with momentum $\mathbf{Q}$ and a bath fermion with momentum $\mathbf{q}$ which are exchanging a momentum $\mathbf{p}$. By using a diagrammatic expansion within the ladder approximation [see Fig. 17(a)], all terms can be resummed to give an implicit equation for the T matrix. Considering, for simplicity, the case of an impurity with zero momentum $Q = 0$, one obtains the follow-
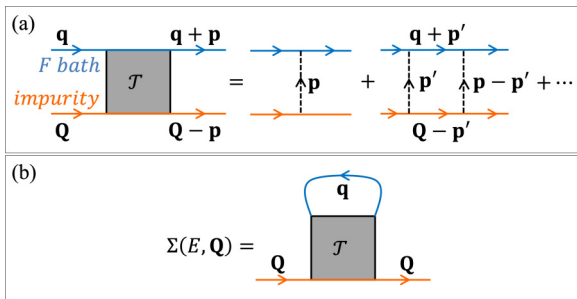

FIG. 17. (a) Ladder diagrams for the T matrix describing the scattering between an impurity with momentum $\mathbf{Q}$ and a particle of the bath with momentum $\mathbf{q}$, which are exchanging a momentum $\mathbf{p}$. (b) Impurity self-energy in terms of the T matrix.

ing implicit equation for the T matrix:

$$\mathcal{T}_{\mathbf{qp}}(E) = V_p + \sum_{\mathbf{p}'} \frac{(1 - f_{\mathbf{q}+\mathbf{p}'})V_{|\mathbf{p}-\mathbf{p}'|}\mathcal{T}_{\mathbf{qp}'}(E)}{E + \epsilon_\mathbf{q} - \epsilon_{\mathbf{p}'} - \epsilon_{\mathbf{q}+\mathbf{p}'}}. \quad \text{(B1)}$$

Here, $f_\mathbf{k}$ is the Fermi-Dirac distribution, i.e., at zero temperature $f_\mathbf{k} = \Theta(k_F - k)$, and $E + \epsilon_\mathbf{q}$ is the initial energy of the scattering process.

Starting from the T matrix, one can evaluate the entire polaron spectrum by evaluating the impurity Green's function in terms of the self-energy—see Fig. 17(b):

$$G(\omega) = \frac{1}{\omega - \Sigma(\omega)}, \quad \text{(B2a)}$$

$$\Sigma(\omega) = \sum_\mathbf{q} f_\mathbf{q} \mathcal{T}_{\mathbf{q},\mathbf{p}=\mathbf{0}}(\omega + i\eta). \quad \text{(B2b)}$$

The spectral function is then obtained from the Green's function as in Eq. (21b).

The T matrix can also be obtained directly from the polaron eigenvalue equations (20). Defining

$$\mathcal{S}_{\mathbf{kq}}(E) \equiv (E - E_{\mathbf{kq}})\frac{\phi_{\mathbf{kq}}}{\phi_0}, \quad \text{(B3)}$$

Eq. (20b) becomes

$$\mathcal{S}_{\mathbf{kq}}(E) = V_{|\mathbf{k}-\mathbf{q}|} + \sum_{\mathbf{k}'} (1 - f_{\mathbf{k}'})V_{|\mathbf{k}-\mathbf{k}'|}\frac{\mathcal{S}_{\mathbf{k}'\mathbf{q}}(E)}{E - E_{\mathbf{k}'\mathbf{q}}}$$
$$- \sum_{\mathbf{q}'} f_{\mathbf{q}'} V_{|\mathbf{q}-\mathbf{q}'|}\frac{\mathcal{S}_{\mathbf{kq}'}(E)}{E - E_{\mathbf{kq}'}}. \quad \text{(B4)}$$

If one neglects the last term, this equation coincides with Eq. (B1) by changing variable $\mathbf{k}' = \mathbf{q} + \mathbf{p}'$ and redefining

$$\mathcal{S}_{\mathbf{q}+\mathbf{p}',\mathbf{q}}(E) = \mathcal{T}_{\mathbf{qp}'}(E). \quad \text{(B5)}$$

The last term in Eq. (B4) describes the scattering of the impurity with a hole of the fermionic bath and corresponds to the $-\sum_{\mathbf{q}'} V_{|\mathbf{q}-\mathbf{q}'|}\phi_{\mathbf{kq}'}$ term in the polaron eigenvalue equations (20). For a contact-interaction potential, the terms $-\sum_{\mathbf{q}'} V_{|\mathbf{q}-\mathbf{q}'|}\phi_{\mathbf{kq}'}$ can be safely neglected [65] because the phase space for hole scattering is small. However, this is not always true for a longer-range potential such as the interlayer dipolar potential.

To show this, we plot in Fig. 18 the lowest polaron energy as well as the entire polaron spectrum, comparing the results of three methods: (i) by solving the polaron eigenvalue problem (20), (ii) by neglecting the term $-\sum_{\mathbf{q}'} V_{|\mathbf{q}-\mathbf{q}'|}\phi_{\mathbf{kq}'}$ in Eq. (20), and (iii) by numerically solving the T-matrix equation (B1) (see below). Methods (ii) and (iii) give exactly the same results, as they should. However, there is a non-negligible shift compared with the results obtained with method (i) if either E_F is large, $E_F \gg E_0$, or if $U_0 > 1$. This coincides with the regime where the interlayer dipolar potential gives a very different scattering phase shift to that of the contact potential—see Appendix A. In particular, the solution of the full problem without neglecting the $-\sum_{\mathbf{q}'} V_{|\mathbf{q}-\mathbf{q}'|}\phi_{\mathbf{kq}'}$ term is always blueshifted in energy compared with the case where one neglects the scattering of the impurity with the holes in the Fermi sea. This shift increases both as a function of U_0 and E_F. If U_0 is large, $U_0 > 1$, as in Fig. 18, then
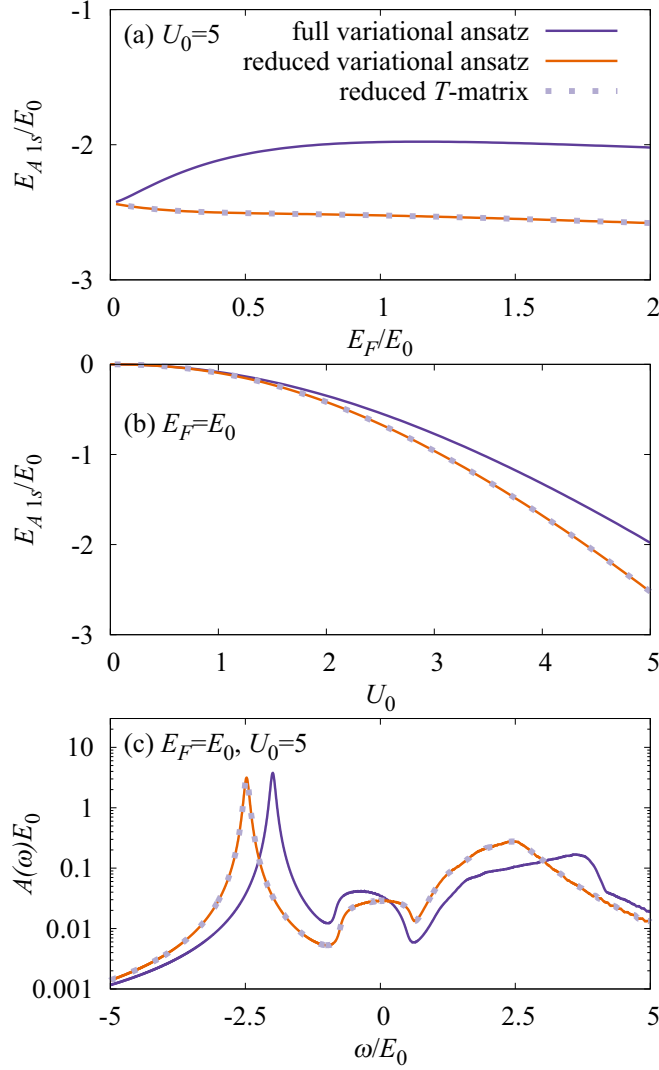
FIG. 18. Polaron properties evaluated in three different ways: (1) by solving the polaron eigenvalue problem (20) (full variational ansatz), (2) by neglecting the $-\sum_{\mathbf{q}'} V_{|\mathbf{q}-\mathbf{q}'|}\phi_{\mathbf{kq}'}$ term describing the scattering with holes (reduced variational ansatz), and (3) by solving the T-matrix equation (B1) by inversion. (a), (b) Energy of the polaron $1s$ attractive branch for (a) $U_0 = 5$ as a function of E_F and (b) $E_F = E_0$ as a function of U_0. (c) Entire polaron spectrum as a function of ω for $E_F = E_0$ and $U_0 = 5$.

the overall redshift of the $1s$ attractive polaron branch as a function of E_F can be changed into a blueshift.

To numerically solve for the T matrix, we can assume that it depends only on a single angle, the one between $\mathbf{q}$ and $\mathbf{p}$ (s-wave ansatz), so that the implicit equation (B1) can be easily solved by direct inversion. If we define vector indices by $i = (p, \varphi)$ and $i' = (p', \varphi')$, the T matrix becomes

$$\mathcal{T}_i(E, q) = \sum_{i'} [\mathbb{I} - \mathbb{K}(E, q)]^{-1}_{ii'} V_{i'},$$

where $V_i = V_p$, and the matrix kernel is

$$\mathbb{K}_{ii'}(E, q) = \frac{dp'p'}{2\pi} \frac{d\varphi'}{2\pi} \frac{(1 - f_{\mathbf{q}+\mathbf{p}'})V_{|\mathbf{p}-\mathbf{p}'|}}{E + \epsilon_{\mathbf{q}} - \epsilon_{\mathbf{p}'} - \epsilon_{\mathbf{q}+\mathbf{p}'}}.$$

Similarly, Eq. (B4) can also be solved by inversion, with the difference that now the vector space has a larger dimension. If we define the vector index as $i = (k, q, \varphi)$, where φ is the angle between $\mathbf{k}$ and $\mathbf{q}$, and if we use the notation $k, k' > k_F$ and $q, q' < k_F$, we find that the T matrix $\mathcal{S}_{\mathbf{kq}}(E)$ can be evaluated as

$$\mathcal{S}_i(E) = \sum_{i'} [\mathbb{I} - \tilde{\mathbb{K}}(E) + \tilde{\mathbb{W}}(E)]^{-1}_{ii'} V_{i'}, \qquad \text{(B6)}$$

where $V_i = V_{|\mathbf{k}-\mathbf{q}|}$, and where the two kernels are

$$\tilde{\mathbb{K}}_{ii'}(E) = \frac{dk'k'}{2\pi} \frac{d\varphi'}{2\pi} dq' \delta(q - q') \frac{V_{|\mathbf{k}-\mathbf{k}'|}}{E - E_{\mathbf{k}'\mathbf{q}}},$$

$$\tilde{\mathbb{W}}_{ii'}(E) = \frac{dq'q'}{2\pi} \frac{d\varphi'}{2\pi} dk' \delta(k - k') \frac{V_{|\mathbf{q}-\mathbf{q}'|}}{E - E_{\mathbf{kq}'}}.$$

The variational ansatz thus allows repeated impurity-hole scattering, unlike the T-matrix formulation. Note that this is qualitatively different from screening effects such as the Gork'ov–Melik-Barkhudarov particle-hole screening of the particle-particle correlations responsible for superfluidity in the BCS-BEC crossover [85]. In particular, an additional excitation would be required to screen the interactions between the impurity and a fermion from the medium. This would be an interesting future direction of research but is beyond the scope of the current work.

[1] T. Lahaye, C. Menotti, L. Santos, M. Lewenstein, and T. Pfau, The physics of dipolar bosonic quantum gases, Rep. Prog. Phys. **72**, 126401 (2009).

[2] M. A. Baranov, M. Dalmonte, G. Pupillo, and P. Zoller, Condensed matter theory of dipolar quantum gases, Chem. Rev. **112**, 5012 (2012).

[3] L. Chomaz, I. Ferrier-Barbut, F. Ferlaino, B. Laburthe-Tolra, B. L. Lev, and T. Pfau, Dipolar physics: A review of experiments with magnetic quantum gases, Rep. Prog. Phys. **86**, 026401 (2023).

[4] A. Griesmaier, J. Werner, S. Hensler, J. Stuhler, and T. Pfau, Bose-Einstein condensation of chromium, Phys. Rev. Lett. **94**, 160401 (2005).

[5] J. Stuhler, A. Griesmaier, T. Koch, M. Fattori, T. Pfau, S. Giovanazzi, P. Pedri, and L. Santos, Observation of dipole-dipole interaction in a degenerate quantum gas, Phys. Rev. Lett. **95**, 150406 (2005).

[6] M. Lu, N. Q. Burdick, S. H. Youn, and B. L. Lev, Strongly dipolar Bose-Einstein condensate of dysprosium, Phys. Rev. Lett. **107**, 190401 (2011).

[7] M. Lu, N. Q. Burdick, and B. L. Lev, Quantum degenerate dipolar Fermi gas, Phys. Rev. Lett. **108**, 215301 (2012).

[8] K. Aikawa, A. Frisch, M. Mark, S. Baier, A. Rietzler, R. Grimm, and F. Ferlaino, Bose-Einstein condensation of erbium, Phys. Rev. Lett. **108**, 210401 (2012).

[9] K. Aikawa, A. Frisch, M. Mark, S. Baier, R. Grimm, J. L. Bohn, D. S. Jin, G. M. Bruun, and F. Ferlaino, Anisotropic relaxation dynamics in a dipolar Fermi gas driven out of equilibrium, Phys. Rev. Lett. **113**, 263201 (2014).

[10] F. Böttcher, J.-N. Schmidt, J. Hertkorn, K. S. H. Ng, S. D. Graham, M. Guo, T. Langen, and T. Pfau, New states of matter with fine-tuned interactions: Quantum droplets and dipolar supersolids, Rep. Prog. Phys. **84**, 012403 (2021).

[11] R. Löw, H. Weimer, J. Nipper, J. B. Balewski, B. Butscher, H. P. Büchler, and T. Pfau, An experimental and theoretical guide to strongly interacting Rydberg gases, J. Phys. B: At. Mol. Opt. Phys. **45**, 113001 (2012).

[12] S. Moses, J. Covey, M. Miecnikowski, D. Jin, and J. Ye, New frontiers for quantum gases of polar molecules, Nat. Phys. **13**, 13 (2017).

[13] J. P. Shaffer, S. T. Rittenhouse, and H. R. Sadeghpour, Ultracold Rydberg molecules, Nat. Commun. **9**, 1965 (2018).

[14] G. Valtolina, K. Matsuda, W. G. Tobias, J.-R. Li, L. De Marco, and J. Ye, Dipolar evaporation of reactive molecules to below the Fermi temperature, Nature (London) **588**, 239 (2020).

[15] L. D. Marco, G. Valtolina, K. Matsuda, W. G. Tobias, J. P. Covey, and J. Ye, A degenerate Fermi gas of polar molecules, Science **363**, 853 (2019).

[16] W. G. Tobias, K. Matsuda, G. Valtolina, L. De Marco, J.-R. Li, and J. Ye, Thermalization and sub-Poissonian density fluctuations in a degenerate molecular Fermi gas, Phys. Rev. Lett. **124**, 033401 (2020).

[17] A. Schindewolf, R. Bause, X.-Y. Chen, M. Duda, T. Karman, I. Bloch, and X.-Y. Luo, Evaporation of microwave-shielded polar molecules to quantum degeneracy, Nature (London) **607**, 677 (2022).

[18] M. Duda, X.-Y. Chen, A. Schindewolf, R. Bause, J. von Milczewski, R. Schmidt, I. Bloch, and X.-Y. Luo, Transition from a polaronic condensate to a degenerate Fermi gas of heteronuclear molecules, Nat. Phys. **19**, 720 (2023).

[19] J. Deiglmayr, A. Grochola, M. Repp, K. Mörtlbauer, C. Glück, J. Lange, O. Dulieu, R. Wester, and M. Weidemüller, Formation of ultracold polar molecules in the rovibrational ground state, Phys. Rev. Lett. **101**, 133004 (2008).

[20] M. Repp, R. Pires, J. Ulmanis, R. Heck, E. D. Kuhnle, M. Weidemüller, and E. Tiemann, Observation of interspecies ^{6}Li - ^{133}Cs Feshbach resonances, Phys. Rev. A **87**, 010701(R) (2013).

[21] J. J. Park, Y.-K. Lu, A. O. Jamison, T. V. Tscherbul, and W. Ketterle, A Feshbach resonance in collisions between triplet ground-state molecules, Nature (London) **614**, 54 (2023).

[22] W. G. Tobias, K. Matsuda, J.-R. Li, C. Miller, A. N. Carroll, T. Bilitewski, A. M. Rey, and J. Ye, Reactions between layer-resolved molecules mediated by dipolar spin exchange, Science **375**, 1299 (2022).

[23] N. R. Cooper and G. V. Shlyapnikov, Stable topological superfluid phase of ultracold polar fermionic molecules, Phys. Rev. Lett. **103**, 155302 (2009).

[24] J. Levinsen, N. R. Cooper, and G. V. Shlyapnikov, Topological $p_x + ip_y$ superfluid phase of fermionic polar molecules, Phys. Rev. A **84**, 013603 (2011).

[25] G. M. Bruun and E. Taylor, Quantum phases of a two-dimensional dipolar Fermi gas, Phys. Rev. Lett. **101**, 245301 (2008).

[26] Y. Yamaguchi, T. Sogo, T. Ito, and T. Miyakawa, Density-wave instability in a two-dimensional dipolar Fermi gas, Phys. Rev. A **82**, 013643 (2010).

[27] K. Sun, C. Wu, and S. Das Sarma, Spontaneous inhomogeneous phases in ultracold dipolar Fermi gases, Phys. Rev. B **82**, 075105 (2010).

[28] M. M. Parish and F. M. Marchetti, Density instabilities in a two-dimensional dipolar Fermi gas, Phys. Rev. Lett. **108**, 145304 (2012).

[29] N. Matveeva and S. Giorgini, Liquid and crystal phases of dipolar fermions in two dimensions, Phys. Rev. Lett. **109**, 200401 (2012).

[30] F. M. Marchetti and M. M. Parish, Density-wave phases of dipolar fermions in a bilayer, Phys. Rev. B **87**, 045110 (2013).

[31] M. Klawunn, J. Duhme, and L. Santos, Bose-Fermi mixtures of self-assembled filaments of fermionic polar molecules, Phys. Rev. A **81**, 013604 (2010).

[32] A. C. Potter, E. Berg, D.-W. Wang, B. I. Halperin, and E. Demler, Superfluidity and dimerization in a multilayered system of fermionic polar molecules, Phys. Rev. Lett. **105**, 220406 (2010).

[33] A. Pikovski, M. Klawunn, G. V. Shlyapnikov, and L. Santos, Interlayer superfluidity in bilayer systems of fermionic polar molecules, Phys. Rev. Lett. **105**, 215302 (2010).

[34] M. Klawunn, A. Pikovski, and L. Santos, Two-dimensional scattering and bound states of polar molecules in bilayers, Phys. Rev. A **82**, 044701 (2010).

[35] A. Mazloom and S. H. Abedinpour, Interplay of interlayer pairing and many-body screening in a bilayer of dipolar fermions, Phys. Rev. B **98**, 014513 (2018).

[36] A. Mazloom and S. H. Abedinpour, Superfluidity in density imbalanced bilayers of dipolar fermions, Phys. Rev. B **96**, 064513 (2017).

[37] H. Lee, S. I. Matveenko, D.-W. Wang, and G. V. Shlyapnikov, Fulde-Ferrell-Larkin-Ovchinnikov state in bilayer dipolar systems, Phys. Rev. A **96**, 061602(R) (2017).

[38] M. Klawunn and A. Recati, Polar molecules in bilayers with high population imbalance, Phys. Rev. A **88**, 013633 (2013).

[39] N. Matveeva and S. Giorgini, Impurity problem in a bilayer system of dipoles, Phys. Rev. Lett. **111**, 220405 (2013).

[40] R. Bombín, T. Comparin, G. Bertaina, F. Mazzanti, S. Giorgini, and J. Boronat, Two-dimensional repulsive Fermi polarons with short- and long-range interactions, Phys. Rev. A **100**, 023608 (2019).

[41] S. Zöllner, G. M. Bruun, and C. J. Pethick, Polarons and molecules in a two-dimensional Fermi gas, Phys. Rev. A **83**, 021603(R) (2011).

[42] M. M. Parish, Polaron-molecule transitions in a two-dimensional Fermi gas, Phys. Rev. A **83**, 051603(R) (2011).

[43] R. Schmidt, T. Enss, V. Pietilä, and E. Demler, Fermi polarons in two dimensions, Phys. Rev. A **85**, 021602(R) (2012).

[44] V. Ngampruetikorn, J. Levinsen, and M. M. Parish, Repulsive polarons in two-dimensional Fermi gases, Europhys. Lett. **98**, 30005 (2012).

[45] M. M. Parish and J. Levinsen, Highly polarized Fermi gases in two dimensions, Phys. Rev. A **87**, 033616 (2013).

[46] H. Tajima, J. Takahashi, S. I. Mistakidis, E. Nakano, and K. Iida, Polaron problems in ultracold atoms: Role of a Fermi sea across different spatial dimensions and quantum fluctuations of a Bose medium, Atoms **9**, 18 (2021).

[47] M. Sidler, P. Back, O. Cotlet, A. Srivastava, T. Fink, M. Kroner, E. Demler, and A. Imamoglu, Fermi polaron-polaritons in charge-tunable atomically thin semiconductors, Nat. Phys. **13**, 255 (2017).

[48] D. K. Efimkin, E. K. Laird, J. Levinsen, M. M. Parish, and A. H. MacDonald, Electron-exciton interactions in the exciton-polaron problem, Phys. Rev. B **103**, 075417 (2021).

[49] A. Tiene, J. Levinsen, J. Keeling, M. M. Parish, and F. M. Marchetti, Effect of fermion indistinguishability on optical absorption of doped two-dimensional semiconductors, Phys. Rev. B **105**, 125404 (2022).

[50] D. Huang, K. Sampson, Y. Ni, Z. Liu, D. Liang, K. Watanabe, T. Taniguchi, H. Li, E. Martin, J. Levinsen, M. M. Parish, E. Tutuc, D. K. Efimkin, and X. Li, Quantum dynamics of attractive and repulsive polarons in a doped $MoSe_2$ monolayer, Phys. Rev. X **13**, 011029 (2023).

[51] X. L. Yang, S. H. Guo, F. T. Chan, K. W. Wong, and W. Y. Ching, Analytic solution of a two-dimensional hydrogen atom. I. Nonrelativistic theory, Phys. Rev. A **43**, 1186 (1991).

[52] P. Massignan, M. Zaccanti, and G. M. Bruun, Polarons, dressed molecules and itinerant ferromagnetism in ultracold Fermi gases, Rep. Prog. Phys. **77**, 034401 (2014).

[53] F. Scazza, M. Zaccanti, P. Massignan, M. M. Parish, and J. Levinsen, Repulsive Fermi and Bose polarons in quantum gases, Atoms **10**, 55 (2022).

[54] Q. Li, E. H. Hwang, and S. Das Sarma, Collective modes of monolayer, bilayer, and multilayer fermionic dipolar liquid, Phys. Rev. B **82**, 235126 (2010).

[55] L. Du, P. Barral, M. Cantara, J. de Hond, Y.-K. Lu, and W. Ketterle, Atomic physics on a 50 nm scale: Realization of a bilayer system of dipolar atoms, arXiv:2302.07209.

[56] L. D. Carr, D. DeMille, R. V. Krems, and J. Ye, Cold and ultracold molecules: Science, technology and applications, New J. Phys. **11**, 055049 (2009).

[57] V. I. Yudson, M. G. Rozman, and P. Reineker, Bound states of two particles confined to parallel two-dimensional layers and interacting via dipole-dipole or dipole-charge laws, Phys. Rev. B **55**, 5214 (1997).

[58] M. M. Parish, F. M. Marchetti, and P. B. Littlewood, Supersolidity in electron-hole bilayers with a large density imbalance, Europhys. Lett. **95**, 27007 (2011).

[59] O. Cotlet, D. S. Wild, M. D. Lukin, and A. Imamoglu, Rotons in optical excitation spectra of monolayer semiconductors, Phys. Rev. B **101**, 205409 (2020).

[60] A. Tiene, J. Levinsen, M. M. Parish, A. H. MacDonald, J. Keeling, and F. M. Marchetti, Extremely imbalanced two-dimensional electron-hole-photon systems, Phys. Rev. Res. **2**, 023089 (2020).

[61] P. Fulde and R. A. Ferrell, Superconductivity in a strong spin-exchange field, Phys. Rev. **135**, A550 (1964).

[62] A. I. Larkin and Y. N. Ovchinnikov, Nonuniform state of superconductors, Zh. Eksp. Teor. Fiz. **47**, 1136 (1964).

[63] R. Casalbuoni and G. Nardulli, Inhomogeneous superconductivity in condensed matter and QCD, Rev. Mod. Phys. **76**, 263 (2004).

[64] L. Radzihovsky and D. E. Sheehy, Imbalanced Feshbach-resonant Fermi gases, Rep. Prog. Phys. **73**, 076501 (2010).

[65] F. Chevy, Universal phase diagram of a strongly interacting Fermi gas with unbalanced spin populations, Phys. Rev. A **74**, 063628 (2006).

[66] R. Combescot and S. Giraud, Normal state of highly polarized Fermi gases: Full many-body treatment, Phys. Rev. Lett. **101**, 050404 (2008).

[67] R. Combescot, A. Recati, C. Lobo, and F. Chevy, Normal state of highly polarized Fermi gases: Simple many-body approaches, Phys. Rev. Lett. **98**, 180402 (2007).

[68] M. A. Baranov, A. Micheli, S. Ronen, and P. Zoller, Bilayer superfluidity of fermionic polar molecules: Many-body effects, Phys. Rev. A **83**, 043602 (2011).

[69] G. D. Mahan, *Many-Particle Physics* (Kluwer Academic, Plenum Publishers, New York, 2000).

[70] M. Punk and W. Zwerger, Theory of rf-spectroscopy of strongly interacting fermions, Phys. Rev. Lett. **99**, 170404 (2007).

[71] G. Baym, C. J. Pethick, Z. Yu, and M. W. Zwierlein, Coherence and clock shifts in ultracold Fermi gases with resonant interactions, Phys. Rev. Lett. **99**, 190407 (2007).

[72] W. E. Liu, Z.-Y. Shi, M. M. Parish, and J. Levinsen, Theory of radio-frequency spectroscopy of impurities in quantum gases, Phys. Rev. A **102**, 023304 (2020).

[73] T. Smoleński, P. E. Dolgirev, C. Kuhlenkamp, A. Popert, Y. Shimazaki, P. Back, X. Lu, M. Kroner, K. Watanabe, T. Taniguchi, I. Esterlis, E. Demler, and A. Imamoğlu, Signatures of Wigner crystal of electrons in a monolayer semiconductor, Nature (London) **595**, 53 (2021).

[74] Y. Shimazaki, C. Kuhlenkamp, I. Schwartz, T. Smoleński, K. Watanabe, T. Taniguchi, M. Kroner, R. Schmidt, M. Knap, and A. Imamoğlu, Optical signatures of periodic charge distribution in a Mott-like correlated insulator state, Phys. Rev. X **11**, 021027 (2021).

[75] A. Popert, Y. Shimazaki, M. Kroner, K. Watanabe, T. Taniguchi, A. Imamoğlu, and T. Smoleński, Optical sensing of fractional quantum Hall effect in graphene, Nano Lett. **22**, 7363 (2022).

[76] I. Schwartz, Y. Shimazaki, C. Kuhlenkamp, K. Watanabe, T. Taniguchi, M. Kroner, and A. Imamoğlu, Electrically tunable Feshbach resonances in twisted bilayer semiconductors, Science **374**, 336 (2021).

[77] K. Nishimura, E. Nakano, K. Iida, H. Tajima, T. Miyakawa, and H. Yabu, Ground state of the polaron in an ultracold dipolar Fermi gas, Phys. Rev. A **103**, 033324 (2021).

[78] K. Aikawa, S. Baier, A. Frisch, M. Mark, C. Ravensbergen, and F. Ferlaino, Observation of Fermi surface deformation in a dipolar quantum gas, Science **345**, 1484 (2014).

[79] T. Kawamura and Y. Ohashi, Feasibility of a Fulde-Ferrell-Larkin-Ovchinnikov superfluid Fermi atomic gas, Phys. Rev. A **106**, 033320 (2022).

[80] H. Shimahara, Phase fluctuations and Kosterlitz-Thouless transition in two-dimensional Fulde-Ferrell-Larkin-Ovchinnikov superconductors, J. Phys. Soc. Jpn. **67**, 1872 (1998).

[81] A. Tiene, A. Tamargo Bracho, M. M. Parish, J. Levinsen, and F. M. Marchetti, Dataset for "Multiple polaron quasiparticles with dipolar fermions in a bilayer geometry", https://doi.org/10.21950/UTHVWP (2024).

[82] P. M. Morse and W. P. Allis, The effect of exchange on the scattering of slow electrons from atoms, Phys. Rev. **44**, 269 (1933).

[83] M. Portnoi and I. Galbraith, Variable-phase method and Levinson's theorem in two dimensions: Application to a screened Coulomb potential, Solid State Commun. **103**, 325 (1997).

[84] J. Levinsen and M. M. Parish, Strongly interacting two-dimensional Fermi gases, Annu. Rev. Cold At. Mol. **3**, 1 (2015).

[85] L. Pisani, A. Perali, P. Pieri, and G. C. Strinati, Entanglement between pairing and screening in the Gorkov-Melik-Barkhudarov correction to the critical temperature throughout the BCS-BEC crossover, Phys. Rev. B **97**, 014528 (2018).